



University of Kentucky
UKnowledge

Theses and Dissertations--Biomedical
Engineering

Biomedical Engineering


2019

CALIBRATED SHORT TR RECOVERY MRI FOR RAPID MEASUREMENT OF BRAIN-BLOOD PARTITION COEFFICIENT AND CORRECTION OF QUANTITATIVE CEREBRAL BLOOD FLOW

Scott William Thalman

University of Kentucky, scott.thalman@uky.edu

Author ORCID Identifier:

 <https://orcid.org/0000-0003-4652-5235>

Digital Object Identifier: <https://doi.org/10.13023/etd.2019.333>

[Right click to open a feedback form in a new tab to let us know how this document benefits you.](#)

Recommended Citation

Thalman, Scott William, "CALIBRATED SHORT TR RECOVERY MRI FOR RAPID MEASUREMENT OF BRAIN-BLOOD PARTITION COEFFICIENT AND CORRECTION OF QUANTITATIVE CEREBRAL BLOOD FLOW" (2019). *Theses and Dissertations--Biomedical Engineering*. 59.
https://uknowledge.uky.edu/cbme_etds/59

This Doctoral Dissertation is brought to you for free and open access by the Biomedical Engineering at UKnowledge. It has been accepted for inclusion in Theses and Dissertations--Biomedical Engineering by an authorized administrator of UKnowledge. For more information, please contact UKnowledge@lsv.uky.edu.

STUDENT AGREEMENT:

I represent that my thesis or dissertation and abstract are my original work. Proper attribution has been given to all outside sources. I understand that I am solely responsible for obtaining any needed copyright permissions. I have obtained needed written permission statement(s) from the owner(s) of each third-party copyrighted matter to be included in my work, allowing electronic distribution (if such use is not permitted by the fair use doctrine) which will be submitted to UKnowledge as Additional File.

I hereby grant to The University of Kentucky and its agents the irrevocable, non-exclusive, and royalty-free license to archive and make accessible my work in whole or in part in all forms of media, now or hereafter known. I agree that the document mentioned above may be made available immediately for worldwide access unless an embargo applies.

I retain all other ownership rights to the copyright of my work. I also retain the right to use in future works (such as articles or books) all or part of my work. I understand that I am free to register the copyright to my work.

REVIEW, APPROVAL AND ACCEPTANCE

The document mentioned above has been reviewed and accepted by the student's advisor, on behalf of the advisory committee, and by the Director of Graduate Studies (DGS), on behalf of the program; we verify that this is the final, approved version of the student's thesis including all changes required by the advisory committee. The undersigned agree to abide by the statements above.

Scott William Thalman, Student

Dr. Ai-Ling Lin, Major Professor

Dr. Abhijit Patwardhan, Director of Graduate Studies

CALIBRATED SHORT TR RECOVERY MRI FOR RAPID MEASUREMENT OF
BRAIN-BLOOD PARTITION COEFFICIENT AND CORRECTION OF
QUANTITATIVE CEREBRAL BLOOD FLOW

DISSERTATION

A dissertation submitted in partial fulfillment of the
requirements for the degree of Doctor of Philosophy in the
College of Engineering
at the University of Kentucky

By

Scott William Thalman
Lexington, Kentucky

Co- Directors: Dr. Ai-Ling Lin, Associate Professor of Biomedical Engineering
and Dr. Guoqiang Yu, Professor of Biomedical Engineering
Lexington, Kentucky

2019

Copyright © Scott William Thalman 2019
<https://orcid.org/0000-0003-4652-5235>

ABSTRACT OF DISSERTATION

CALIBRATED SHORT TR RECOVERY MRI FOR RAPID MEASUREMENT OF BRAIN-BLOOD PARTITION COEFFICIENT AND CORRECTION OF QUANTITATIVE CEREBRAL BLOOD FLOW

The high prevalence and mortality of cerebrovascular disease has led to the development of several methods to measure cerebral blood flow (CBF) in vivo. One of these, arterial spin labeling (ASL), is a quantitative magnetic resonance imaging (MRI) technique with the advantage that it is completely non-invasive. The quantification of CBF using ASL requires correction for a tissue specific parameter called the brain-blood partition coefficient (BBPC). Despite regional and inter-subject variability in BBPC, the current recommended implementation of ASL uses a constant assumed value of 0.9 mL/g for all regions of the brain, all subjects, and even all species.

The purpose of this dissertation is 1) to apply ASL to a novel population to answer an important clinical question in the setting of Down syndrome, 2) to demonstrate proof of concept of a rapid technique to measure BBPC in mice to improve CBF quantification, and 3) to translate the correction method by applying it to a population of healthy canines using equipment and parameters suitable for use with humans.

Chapter 2 reports the results of an ASL study of adults with Down syndrome (DS). This population is unique for their extremely high prevalence of Alzheimer's disease (AD) and very low prevalence of systemic cardiovascular risk factors like atherosclerosis and hypertension. This prompted the hypothesis that AD pathology would lead to the development of perfusion deficits in people with DS despite their healthy cardiovascular profile. The results demonstrate that perfusion is not compromised in DS participants until the middle of the 6th decade of life after which measured global CBF was reduced by 31% ($p=0.029$). There was also significantly higher prevalence of residual arterial signal in older participants with DS (60%) than younger DS participants (7%, $p = 0.005$) or non-DS controls (0%, $p < 0.001$). This delayed pattern of perfusion deficits in people with DS differs from observations in studies of sporadic AD suggesting that adults with DS benefit from an improved cardiovascular risk profile early in life.

Chapter 3 introduces calibrated short TR recovery (CaSTRR) imaging as a rapid method to measure BBPC and its development in mice. This was prompted by the inability to account for potential changes in BBPC due to age, brain atrophy, or the accumulation of hydrophobic A- β plaques in the ASL study of people with DS in Chapter 2. The CaSTRR method reduces acquisition time of BBPC maps by 87% and measures a significantly higher BBPC in cortical gray matter (0.99 ± 0.04 mL/g,) than white matter in the corpus callosum (0.93 ± 0.05 mL/g, $p=0.03$). Furthermore, when CBF maps are corrected for

BBPC, the contrast between gray and white matter regions of interest is improved by 14%. This demonstrates proof of concept for the CaSTRR technique.

Chapter 4 describes the application of CaSTRR on healthy canines (age 5-8 years) using a 3T human MRI scanner. This represents a translation of the technique to a setting suitable for use with a human subject. Both CaSTRR and pCASL acquisitions were performed and further optimization brought the acquisition time of CaSTRR down to 4 minutes which is comparable to pCASL. Results again show higher BBPC in gray matter (0.83 ± 0.05 mL/g) than white matter (0.78 ± 0.04 mL/g, $p = 0.007$) with both values unaffected by age over the range studied. Also, gray matter CBF is negatively correlated with age ($p = 0.003$) and BBPC correction improved the contrast to noise ratio by 3.6% (95% confidence interval = 0.6 – 6.5%).

In summary, the quantification of ASL can be improved using BBPC maps derived from the novel, rapid CaSTRR technique.

KEYWORDS: Cerebral Blood Flow, Arterial Spin Labeling, Brain-Blood Partition Coefficient, Magnetic Resonance Imaging, Calibrated Short TR Recovery

Scott William Thalman

(Name of Student)

05/29/2019

Date

CALIBRATED SHORT TR RECOVERY MRI FOR RAPID MEASUREMENT OF
BRAIN-BLOOD PARTITION COEFFICIENT AND CORRECTION OF
QUANTITATIVE CEREBRAL BLOOD FLOW

By
Scott William Thalman

Dr. Ai-Ling Lin

Co-Director of Dissertation

Dr. Guoqiang Yu

Co-Director of Dissertation

Dr. Abhijit Patwardhan

Director of Graduate Studies

05/29/2019

To Jackson, Eli, and Charlotte.

“Seek ye out of the best books words of wisdom;
seek learning, even by study and also by faith.”

D&C 88:118

ACKNOWLEDGMENTS

My first and eternal gratitude will always be to my wife, Lesley. If there is anything great I have achieved in my life it is because I married her. She sees a hero in me and with her endless love and support, each day I get closer to becoming one.

I owe a great deal to Dr. Ai-Ling Lin, my mentor. She came into my life at a time when I was struggling and gave me a second chance. Her support and patience have made this project possible, and her lab has been a tremendous source of joy and accomplishment. I have no doubt that many prayers have been answered during the time we have been able to work together.

I would also like to thank Dr. David Powell. He has been instrumental to my understanding of MRI and I couldn't have done this without him. I have thoroughly enjoyed the time I got to spend with him in the MRISC.

I am very grateful to the rest of my dissertation committee. Dr. Guoqiang Yu for his encouragement to develop my talents as an engineer. Dr. Peter Nelson for always asking, "Why does this matter?" and reminding me to focus on what's really important. And Dr. Brian Gold, whose questions were always meant to make my science better. I would also like to thank Dr. Peter Hardy for taking the time to serve as my outside examiner and lend his expertise to my dissertation.

I have had the wonderful fortune of working with many exceptional students and post-doctoral fellows and I want to recognize their influence and help on this project. Dr. Ishita Parikh., Dr. Jared Hoffman, and Vikas Bakshi showed me the ropes in small animal neuroimaging. They read my abstracts and papers, and their hard work was an incredible

example of dedication and fun. Tyler Hammond, Lucy Yanckello, and Mengfan Xia make the Lin Lab a joy to work in each day with their excitement and encouragement. Margo Ubele was a tremendous help in working with the dogs and I'm grateful she was willing to let me hijack her experiment. Dr. Kate Van Pelt really helped push the Down syndrome paper over the top and I'm grateful for her help in checking and double checking my work, particularly in statistics.

Of all the students I worked with I don't think there were any that meant as much to me as Dr. Greg Wehner. He was my model for success throughout this program, and I benefited many times from his exceptional insight. Greg is the very definition of constructive criticism, and more than that a fantastic friend.

The collaboration with Dr. Fred Schmitt and Dr. Liz Head on the Down syndrome paper was a joy to participate in. They have incredible insight and listening to them generate new hypotheses and ways to test them was always inspiring.

I have received exceptional training through the F. Joseph Halcomb III, M.D. Fellowship for Engineering in Medicine and the Sanders-Brown Center on Aging T32 Fellowship. Dr. Halcomb is inspiring for his generosity and his desire to support future scientist, and he supported me through a difficult transition. I would also like to thank Dr. Linda Van Eldik for her work in the T32 program and encouraging me to do the best science I could.

I particularly want to thank the volunteers and their families who were willing to give of their precious time to participate in the long term Down syndrome study. This work would be impossible without them and they are truly the MVPs of our research team.

I want to acknowledge the University of Kentucky MD/PhD program as well. Getting a phone call from Therese Stearns encouraging me to send in a secondary application to the program was one of the defining moments in my life and set me on an amazing adventure here in Kentucky. She has become a part of my family, and her support, particularly when I was struggling, has meant the world to me. Dr. Susan Smythe has been a remarkable example and mentor. She has been an advocate, an advisor, and a teacher of the highest order, and I am grateful every day that she saw excellence in me.

Finally, I want to thank my amazing parents, Gary and Cyndi, and my wonderful siblings, Josh, Abbey, and Tyler. Every morning when I left the house my father reminded me to “be smart.” That phrase has always meant more to me than just my education because I had his example of tireless work, selfless service, and righteous choices to show me what “smart” really means. I have never had sufficient words of gratitude that would do justice to the level of care, support, and sacrifice my mother has shown me, so I will write only what I can; thank you. My brothers and sister have always been my closest friends, my fiercest fans, and the ones who will never let me forget that my fancy degrees won’t do me any good if I end up on the wrong side of the gate. Truly, all the world is filled with love, when there’s love at home.

TABLE OF CONTENTS

ACKNOWLEDGMENTS	III
TABLE OF CONTENTS	VI
LIST OF TABLES	IX
LIST OF FIGURES	X
CHAPTER 1. INTRODUCTION	1
1.1 CEREBRAL BLOOD FLOW	1
1.2 PERFUSION IMAGING TECHNIQUES.....	2
1.3 ARTERIAL SPIN LABELING	3
1.3.1 <i>Development</i>	3
1.3.2 <i>Applications</i>	4
1.3.3 <i>Weaknesses</i>	4
1.4 ARTERIAL SPIN LABELING QUANTIFICATION.....	5
1.4.1 <i>Kety-Schmidt Equation and Tracer Kinetics</i>	5
1.4.2 <i>Assumptions</i>	8
1.5 BRAIN-BLOOD PARTITION COEFFICIENT.....	8
1.5.1 <i>Role of BBPC</i>	8
1.5.2 <i>Variability in BBPC</i>	9
1.5.3 <i>Current Standards for BBPC in ASL</i>	10
1.6 DISSERTATION OBJECTIVES	10
CHAPTER 2. GLOBAL CEREBRAL BLOOD FLOW IN PEOPLE WITH DOWN SYNDROME	13
2.1 INTRODUCTION	13
2.2 METHODS	14
2.2.1 <i>Participants</i>	14
2.2.2 <i>ASL Methods and Analysis</i>	16
2.2.3 <i>Residual Arterial Signal Scoring</i>	17
2.2.4 <i>Statistics</i>	18
2.3 RESULTS	19
2.3.1 <i>Demographic Characteristics</i>	19

2.3.2	<i>Cerebral Blood Flow vs Age</i>	20
2.3.3	<i>Severe RAS and Dementia in People with DS</i>	22
2.4	DISCUSSION	23
CHAPTER 3. NOVEL CALIBRATED SHORT TR RECOVERY (CASTRR) METHOD FOR BRAIN-BLOOD PARTITION COEFFICIENT CORRECTION IN MICE 29		
3.1	INTRODUCTION	29
3.2	METHODS	30
3.2.1	<i>Animal Model</i>	30
3.2.2	<i>Calibrated Short TR Recovery Imaging Protocol</i>	32
3.2.3	<i>Pseudo-Continuous ASL Protocol</i>	34
3.2.4	<i>Image Analysis</i>	35
3.2.5	<i>Statistics</i>	35
3.3	RESULTS	35
3.3.1	<i>Corpus Callosum Demonstrates Reduced BBPC Compared To Neocortex</i> 35	
3.3.2	<i>Corpus Callosum Demonstrates Lower Perfusion than Gray Matter</i>	37
3.3.3	<i>Corrected CBF Maps Demonstrate Greater Contrast than Uncorrected</i> ..	38
3.4	DISCUSSION	39
CHAPTER 4. BRAIN-BLOOD PARTITION COEFFICIENT AND CEREBRAL BLOOD FLOW IN CANINES USING CALIBRATED SHORT TR RECOVERY (CASTRR) CORRECTION METHOD..... 43		
4.1	INTRODUCTION	43
4.2	METHODS	44
4.2.1	<i>Animal Model</i>	44
4.2.2	<i>Scanning procedure</i>	45
4.2.3	<i>Calibrated Short TR Recovery Imaging</i>	45
4.2.4	<i>Cerebral Blood Flow and Anatomical Imaging</i>	48
4.2.5	<i>Image Analysis</i>	49
4.2.6	<i>Statistical Analysis</i>	49
4.3	RESULTS	50
4.3.1	<i>BBPC is Higher in Gray Matter than in White Matter</i>	50
4.3.2	<i>Gray Matter CBF is Negatively Correlated with Age</i>	51
4.3.3	<i>BBPC Correction improves contrast to noise ratio in CBF maps</i>	52

4.3.4 <i>BBPC Values Generated Using Hematocrit Agree with Values Generated Using Phantoms</i>	53
4.4 DISCUSSION	54
CHAPTER 5. DISCUSSION	58
5.1 OVERVIEW	58
5.2 FUTURE DIRECTIONS.....	59
5.3 INNOVATION	61
5.4 CONCLUSION.....	62
REFERENCES	63
VITA	72

LIST OF TABLES

Table 2.1 Demographics	19
Table 3.1 Mean Partition Coefficient and Perfusion Values by Region	36

LIST OF FIGURES

Figure 2.1 Representative CBF maps demonstrating residual arterial signal (RAS)	18
Figure 2.2 Global CBF versus participant age.....	21
Figure 2.3 Mean global CBF	22
Figure 3.1 Explanation of the calibrated short repetition time recovery (CaSTRR) imaging protocol to measure BBPC.....	32
Figure 3.2 Representative maps of BBPC and CBF.	37
Figure 3.3 Regional analysis of BBPC.....	37
Figure 3.4 CBF by Region	38
Figure 3.5 Improved contrast from BBPC correction.....	39
Figure 4.1 Explanation of CaSTRR and pCASL methods used in this study.	46
Figure 4.2 Average BBPC vs Age.	50
Figure 4.3 Gray and White CBF versus Age.....	52
Figure 4.4 Correlation of BBPC values.....	54

CHAPTER 1. INTRODUCTION

1.1 Cerebral Blood Flow

For almost a century, scientists and physicians have been developing non-invasive imaging methods to measure blood flow in the brain [1]. The critical importance of perfusion to physiological function and the abundance of pathologies that can lead to its compromise emphasize the significance of those methods in diagnosing and treating neurological diseases. For example, cerebrovascular disease (CVD) is the second leading cause of death worldwide [2] and the fifth leading cause of death in the United States [3]. Alzheimer's disease (AD) and other dementias represent the fifth leading cause of death globally and sixth in the US [2]. Each year these two causes account for more than 250,000 deaths in the United States and more than 7.5 million deaths worldwide[2, 3].

The applications of perfusion imaging are extremely broad and represent valuable tools in both research and clinical care. In-vivo measurements of cerebral blood flow (CBF) are critical in the management of primary cerebrovascular diseases like acute ischemic stroke [4-6] or arteriovenous malformation [7, 8], with the results determining the administration of tissue plasminogen activator (tPA) [9] or surgical intervention [10]. Cerebral perfusion has also been identified as an important biomarker in studying and monitoring neurodegenerative diseases like Alzheimer's disease [11], frontotemporal lobar degeneration [12], and vascular dementia [13]. In the case of AD it has been shown that individuals with genetic risk factors for dementia demonstrate reduced CBF decades in advance of cognitive impairment [14, 15]. Perfusion imaging is also common outside of the brain, particularly in the heart [16] and kidneys [17], and applications will continue to multiply with the advancement of imaging technologies.

1.2 Perfusion Imaging Techniques

The earliest qualitative images of the cerebrovasculature were X-ray projections which employed iodinated contrast agents injected directly into the carotid artery [1]. Later, quantitative methods were developed to measure CBF based upon the principle of tracer dilution and Fick's principle of mass balance in blood flow. The first qualitative experiments used inhaled tracers such as nitrous oxide (N_2O) or radioactive xenon that were freely diffusible and whose concentration could be measured in the blood of the carotid artery and jugular vein [18, 19]. Quantitative CBF imaging was made possible with the development of X-ray computed tomography (CT) such that tracer concentration measurements could be resolved spatially [20]. Other radiolabeled tracers were developed for use in single-photon emission CT (SPECT) [21] and $H_2^{15}O$ positron emission tomography (PET) [22]. Improvements in the speed of CT scanners has enabled dynamic perfusion imaging using a bolus injection of iodinated contrast agent [23]. All of these techniques are in common use in clinical practice today, but they all share the important disadvantages of invasiveness and exposure to ionizing radiation.

Perfusion imaging methods have also been developed for magnetic resonance imaging (MRI) with the significant advantage that this modality requires no ionizing radiation. The first MRI perfusion technique was dynamic susceptibility contrast (DSC) which used an intravenous injection of chelated gadolinium as an exogenous contrast agent [24]. Later, Williams et al. developed a completely non-invasive method to create perfusion weighted images by labeling the magnetic spins of the hydrogen protons of water molecules in the arterial blood (arterial spins) [25]. The labeled arterial spins would decrease the observed MRI signal relative to a control image where spins were not labelled,

with the difference in signal being proportional to CBF. This technique is called arterial spin labeling (ASL), and it has been the subject of growing interest due to its primary advantage of non-invasiveness.

1.3 Arterial Spin Labeling

1.3.1 Development

The first implementation of ASL used a continuous stream of radiofrequency (RF) excitation and a slice-selective magnetic gradient to invert arterial spins in a narrow plane proximal to the imaging plane. Because the arterial spins are continuously labelled as they pass through the labeling plane this method is known as continuous ASL (CASL). Since the first description of CASL in 1992 numerous improvements have been made to address the various limitations of the early technique. Pulsed ASL (PASL) [26, 27], which uses a short RF pulse to label a thick slab of blood in the neck region, was developed to accommodate the more common RF transmitters that were unable to sustain the high duty cycles necessary for CASL as well as to improve tagging efficiency. Later, pseudo-continuous ASL (pCASL) was developed which used a train of short pulses interspersed with a gradient wave to replicate the adiabatic inversion of CASL with lower RF deposition and less susceptibility to magnetization transfer effects [28]. Like PASL, pCASL does not require special equipment and has the benefit of greater signal to noise ratio (SNR), though not as high as CASL. Improvements were also made to the quantification model to account for arterial transit delays [29]. Due to the flexibility and variety of MRI sequences, there is an abundance of specific implementations within each of these broad categories.

1.3.2 Applications

ASL has been applied to a wide range of normal and pathological conditions including normal aging [30, 31], ischemic injury [32, 33], epilepsy [34, 35], traumatic brain injury [36, 37], AD and other neurodegenerative diseases [12, 38, 39], neural neoplasm [40-42], and arteriovenous malformation [7]. Because there is no requirement for exogenous contrast or ionizing radiation, ASL has been used in pediatric populations [43] to study cerebral perfusion in sickle cell anemia [44] and congenital heart disease [45]. Pre-clinical models of many of these diseases have been studied using ASL in dedicated small animal scanners [46-50]. There are also many examples of ASL perfusion measurements outside of the brain including the kidney [17], pancreas [51] and liver [52]. An important review by Alsop and colleagues describes the current recommended implementation for ASL in clinical applications[53].

1.3.3 Weaknesses

The science of MRI, like many other fields, is composed of trade-offs. While ASL does have the advantage of being quantitative and completely non-invasive, it is a subtractive method and the amount of contrast derived from labeled arterial spins is relatively small. This leads to a low native SNR which must be improved with either large voxels or many averages. Large voxels yield low-resolution images and increasing the number of averages requires longer acquisition times.

Another weakness of ASL arises when applying the quantification model to perfusion weighted images in order to create quantitative maps of CBF. The general kinetic

model is rigorously derived, however, its application typically requires some underlying assumptions to be made in practice.

1.4 Arterial Spin Labeling Quantification

1.4.1 Kety-Schmidt Equation and Tracer Kinetics

To quantify CBF from an ASL acquisition it is necessary to apply a quantification model based on tracer kinetics. The models of tracer diffusion are well established going back to the N₂O experiments of Kety and Schmidt in 1948 [18] and were unified into a general kinetic model for ASL by Buxton and colleagues in 1998 [29]. It was first demonstrated that the change over time in the concentration of a freely diffusible tracer in tissue is equal to the flow multiplied by the difference in concentration between the arterial input and venous output of the tissue. This is known as Fick's principle of cardiac output [54] and can be expressed as,

$$\frac{dc_t(t)}{dt} = f \cdot (c_a(t) - c_v(t)) \quad (1.1)$$

where $c_t(t)$, $c_a(t)$ and $c_v(t)$ are the concentrations of tracer in the tissue, arterial blood, and venous blood respectively and f is the blood flow. If the tracer is well-mixed and freely-diffusible, $c_t(t)$ will be equal to $c_v(t)$ corrected for the relative solubility of the tracer in the tissue and the blood. This correction factor is called the brain-blood partition coefficient (BBPC) and is denoted as λ . Substitution and integration yields,

$$\lambda c_v(t) = c_t(t) = f(t) \cdot \int_0^t (c_a(\tau) - c_v(\tau)) d\tau \quad (1.2)$$

This equation was suitable for the Kety and Schmidt experiment that used continuous exposure to inhaled N₂O to eventually reach a steady state, but it requires modification for use in ASL to account for a finite bolus of tracer, imperfect labeling of arterial spins, and time decay of the magnetic label due to the longitudinal relaxation rate of the blood, $T_{1,b}$. The following describes the derivation of the general kinetic equation for PASL, but it can be adapted to pCASL with only small modifications [29].

In ASL the tracer is hydrogen protons in the water molecules of the blood whose magnetic moments have been inverted. In a control image these arterial spins would add to the measured MRI signal, but in the labelled image the arterial spins have been inverted and therefore any arterial signal that remains after the time decay of the label is subtracted from the MRI signal. Thus, the tissue concentration is equal to half the difference between the control and labeled images:

$$c_t(t) = \Delta M / 2 \quad (1.3)$$

The arterial concentration of label is equal to the product of the maximal equilibrium magnetization of arterial spins, $M_{0,b}$; the labeling efficiency, α ; and the arterial input function, $c(t)$:

$$c_a(t) = \alpha \cdot M_{0,b} \cdot c(t) \quad (1.4)$$

Instead of a venous concentration measurement, a residue function describes the combined washout of tracer from a voxel of interest and time decay of tracer label. This residue function, $r(t)$, is a function of flow, f , partition coefficient, λ , and the T_1 of the tissue:

$$r(t) = e^{-\frac{ft}{\lambda}} \cdot e^{-\frac{t}{T_{1,t}}} \quad (1.5)$$

In this case the tissue concentration which is equivalent to $\Delta M/2$ is expressed as the blood flow, f , times the convolution of the arterial concentration with the residue function to yield the general kinetic equation:

$$\Delta M = 2 \cdot \alpha \cdot M_{0,b} \cdot f \cdot \int_0^t c(t) \cdot r(t - \tau) d\tau \quad (1.6)$$

The arterial input function is a stepwise function which assumes a bolus with well-defined leading and trailing edges and a labeling magnitude that decays with time according to $T_{1,b}$:

$$c(t) = \begin{cases} 0, & t < \tau_a \\ e^{-\frac{t}{T_{1,b}}}, & \tau_a < t < \tau_d \\ 0, & t \geq \tau_d \end{cases} \quad (1.7)$$

where τ_a and τ_d are the arrival times of the leading and trailing edges of the bolus at the voxel of interest.

If the image acquisition is programmed to occur after an inflow time $t = TI > \tau_d$, then Equations 1.4 and 1.5 can be substituted in to Equation 1.6 which is then solved for f yielding,

$$f = \frac{\Delta M}{2 \cdot \alpha \cdot M_{0,b}} \cdot \frac{\delta R}{(1 - e^{-\delta R \cdot (TI - \tau_d)})} \cdot e^{-R_{1,b} \cdot \tau_d} \cdot e^{-R_{1,app} \cdot (TI - \tau_d)} \quad (1.8)$$

where R_1 is the relaxation rate which is the inverse of T_1 , and $R_{1,b}$ is the relaxation rate of blood, $R_{1,app} = R_{1,t} + \frac{f}{\lambda}$ is the apparent relaxation rate of the tissue, and $\delta R = R_{1,b} -$

$R_{1,app}$. In practice the apparent relaxation rate of the tissue is very close to that of the blood such that δR approaches zero. This means Equation 1.8 can be reduced to,

$$f = \frac{\Delta M \cdot e^{\frac{TI}{T_{1,b}}}}{2 \cdot \alpha \cdot M_{0,b} \cdot TI} [mL/g/s] \quad (1.9)$$

1.4.2 Assumptions

The inflow time, TI , is the delay between the initial labeling of arterial spins and image acquisition. This is a scan parameter selected by the operator to be long enough to ensure that the trailing edge of the bolus has had sufficient time to arrive in all voxels in the image volume but not so long that the label has undergone too much time decay. The labeling efficiency, α , has been shown to be 98% in PASL [55] and 85% in pCASL [28]. Ideally the $T_{1,b}$ and $M_{0,b}$ would be measured for each subject, however in practice these values are normally assumed. The error due to $T_{1,b}$ is generally small except in populations where hematocrit can change drastically such as in neonates. The common practice is to assume that $T_{1,b} = 1.65$ s at 3T [56].

1.5 Brain-Blood Partition Coefficient

1.5.1 Role of BBPC

The estimation of $M_{0,b}$ is not as straightforward. The standard of practice is to normalize the ΔM image using a separate proton density weighted acquisition. This is equivalent to dividing each voxel by the equilibrium magnetization of the tissue, $M_{0,t}$,

instead of the blood. The $M_{0,t}$ is then related to the $M_{0,b}$ through the brain-blood partition coefficient by recognizing that,

$$\lambda = \frac{M_{0,t}}{M_{0,b}} \quad (1.10)$$

For PASL, this yields the final quantification equation,

$$f = \frac{6000 \cdot \lambda \cdot \Delta M \cdot e^{\frac{TI}{T_{1,b}}}}{2 \cdot \alpha \cdot M_{0,t} \cdot TI} [mL/100g/min] \quad (1.11)$$

where the number 6000 is a unit conversion from mL/g/s to mL/100g/min [53].

Normalization to a proton density image has the advantage of correcting for inhomogeneities in excitation or in the receiver coil profile. However, the BBPC remains unknown and must be measured or assumed.

1.5.2 Variability in BBPC

The BBPC is a tissue specific parameter which varies greatly across the two main tissue types in the brain. In humans the average BBPC is reported as 0.98 mL/g in gray matter and 0.83 mL/g in white matter [57, 58]. Even among the various gray matter regions BBPC can vary as much as 20% [59]. The BBPC also varies with age, particularly in neonates where brain water content is higher than adults at the same time blood water content is lower than adults [57]. A study using $C^{15}O_2$ PET also demonstrated a 19% decrease in BBPC in regions of cerebral infarction [60]. BBPC can also vary with species with a study in macaques reporting an average gray matter BBPC of 0.78 mL/g [61]. Therefore, BBPC should be determined empirically for each voxel in the image for each subject.

1.5.3 Current Standards for BBPC in ASL

Empirical BBPC measurement has been performed using MRI in both humans and mice using a similar technique [58, 62]. Using a series of fast low-angle shot (FLASH) gradient echo (GRE) acquisitions with varying repetition times (TR), it was possible to determine relative proton density in each voxel. These relative proton density maps were then calibrated to an absolute scale based on a series of phantoms placed alongside the subject's head that were doped with an increasing concentration of deuterium oxide (D_2O) which does not produce MRI signal. Unfortunately, these acquisitions were prohibitively long requiring approximately 30 minutes to acquire a single slice in humans and 130 minutes to acquire ten slices in mice. This is unfeasible in the context of ASL techniques which require 4-6 minutes of acquisition time in humans and 15-20 minutes in mice.

In their consensus report on the recommended implementation of ASL for clinical practice, Alsop and colleagues recommend using an assumed value of 0.9 mL/g instead of a specific BBPC correction [53]. This value represents the whole brain average water content as measured by Herscovitch and Raichle using desiccation of ex-vivo human brain samples [57]. Substituting a single average value for the entire brain into the ASL quantification model disregards the regional and inter-subject variability of BBPC, and represents a known weakness of the ASL technique.

1.6 Dissertation Objectives

The goal of the present work is 1) to describe the application of ASL in a novel population to answer an important clinical question in the setting of Down syndrome, 2) to demonstrate proof of concept of a rapid technique to measure BBPC in mice to improve

CBF quantification, and 3) to translate the correction method by applying it to a population of healthy canines using equipment and parameters suitable for use with humans.

Chapter 2 is a report of an ASL study of adults with trisomy 21 or Down syndrome (DS). This population is particularly important in understanding the role of systemic cardiovascular risk factors on AD. Because amyloid precursor protein (APP) is encoded on chromosome 21, people with DS overexpress APP leading to the development of AD neuropathology as early as the fourth decade of life. The accelerated accumulation of beta amyloid (A- β) is likely one of the causes of the very high prevalence of dementia in people with DS after 50 years of age [63, 64]. In non-DS related AD, cerebrovascular neuropathology is thought to contribute in 6-45% of cases[65] with an observable decrease in CBF as much as two decades prior to the onset of dementia [11]. However, people with DS are protected from key cerebrovascular risk factors like atherosclerosis and hypertension. What was previously unknown was whether the accelerated A- β deposition in people with DS was accompanied by vascular dysfunction. The study in chapter 2 measures global CBF using PASL in a cohort of participants with DS (age 26-65) and non-DS controls (age 26-63). The results suggest that CBF drops significantly in people with DS during the 6th decade of life and other evidence of potential vascular dysfunction develops as well. It is possible that adults with DS benefit from an improved cardiovascular risk profile prior to age 50, but this is eventually overwhelmed by A- β deposition and the development of cerebral amyloid angiopathy (CAA).

In the study described in chapter 2, the participants with DS were experiencing aging effects, brain atrophy, and the deposition of hydrophobic A- β plaques. All of these could potentially change the water balance of the brain and therefore the BBPC. It was not

feasible, however, to account for those changes with the currently available technique to measure BBPC non-invasively. Therefore a new method was developed to measure BBPC with an acquisition time comparable to that of ASL.

Chapter 3 describes the novel, rapid BBPC measurement called calibrated short TR recovery (CaSTRR). The CaSTRR method is based on the previously described FLASH-GRE technique, but reduces the acquisition time by 87%. The results of chapter 3 demonstrate a significantly higher BBPC in cortical gray matter than in the white matter of the corpus callosum and improved contrast between gray and white matter regions of CBF maps when corrected for regional differences in BBPC.

Chapter 4 describes the translation of the CaSTRR method for use with equipment and parameters suitable for use with human subjects. In this study CaSTRR and pCASL acquisitions were performed on a cohort of healthy canines using a 3T human scanner without special equipment. The results show that acquisition time was further reduced to 4 minutes, BBPC did not vary across the age range studied but was significantly higher in gray matter than white matter, and BBPC correction again improved the contrast to noise ratio between gray and white matter regions of the CBF maps. It was also demonstrated that the CaSTRR technique can be further simplified by using hematocrit as a proxy value when calibrating the CaSTRR derived BBPC maps. All of this is evidence of the feasibility of using empirically derived BBPC measurements to improve CBF quantification when using ASL.

CHAPTER 2. GLOBAL CEREBRAL BLOOD FLOW IN PEOPLE WITH DOWN SYNDROME

2.1 Introduction

Down syndrome or trisomy 21 is the most common chromosomal disorder affecting 13.5 of every 10,000 live births and leads to intellectual disability [66-68]. Improved medical care has brought about a significant extension in lifespan and quality of life for people with DS [69, 70]. However, older adults with DS are at high risk for developing dementia, with incidence and prevalence increasing substantially after 50 years of age [63, 64]. Dementia in DS likely arises from Alzheimer's disease (AD) neuropathology. AD neuropathology is typically observed after 30 years of age and involves both beta-amyloid (A β) deposition in plaques and neurofibrillary tangles [71]. The overexpression of APP on chromosome 21 is thought to be a key contributor to AD neuropathology and dementia in DS [72, 73].

Among typically developing individuals, AD commonly co-occurs with cerebrovascular disease (CVD). Estimates of a mixed etiology of AD with CVD range from 5.7-45% in autopsy cases from the general population [65]. The contribution of cerebrovascular disease (CVD) to AD is increasingly being recognized as an important comorbidity that accelerates the age of onset of dementia and also leads to a faster progression of the disease [74, 75]. CVD can serve as a "second hit" necessary to develop clinical signs of dementia particularly when significant A β is present in the brain [76].

DS represents a unique opportunity to study the cerebrovascular features of aging and AD because people with DS exhibit fewer systemic vascular risk factors than those without DS. This population exhibits an absence of atheroma and lower blood pressure

than similarly aged adults without DS [77-79]. While other signs of CVD are rare in DS, cerebral amyloid angiopathy (CAA) has been described [80]. CAA is the deposition of A β in the walls of medium- and small-size leptomeningeal and cortical arteries, arterioles and, less frequently, capillaries and veins [80]. CAA can lead to micro- and macro-hemorrhages [81] and is observed in older individuals with DS [82-84]. Indeed CAA is more frequent in DS relative to older people with sporadic AD [85] and associated with microhemorrhages [86]. Thus, adults with DS represent an important cohort to study the relationship between CVD and AD because while people with DS accumulate CAA, the CAA occurs without atheroma and hypertension.

Arterial spin labeling (ASL) is an advanced quantitative magnetic resonance imaging (MRI) technique that can measure cerebral blood flow (CBF) noninvasively and without the need for exogenous contrast agents [53, 87]. We hypothesized that 1) people with DS would show lower CBF by ASL than similarly aged people without DS and 2) CBF will decrease with age in DS. To test these hypotheses, pulsed ASL was used to acquire quantitative CBF maps from 35 cognitively characterized people with DS ranging in age from 26 to 65 years, with and without dementia. In addition, 15 people without DS ranging in age from 26-63 years served as a non-DS control group (CTL).

2.2 Methods

2.2.1 Participants

ASL measures were collected from a single visit during an ongoing longitudinal study of aging in DS evaluating decline in cognitive functioning and neural integrity as predictors of the development of dementia [88]. We recruited participants older than

25 years through local DS support groups and residential facilities in Kentucky and southern Ohio from 2015-2016. We excluded participants if they had active and unstable medical conditions (e.g., cardiovascular complications). Because thyroid dysfunction is common in individuals with DS, we included these participants if their thyroid dysfunction was medically controlled. People with DS who were demented may have also been prescribed AD medications, and these individuals were also included in the study. Upon request, 13 participants were provided with Ativan to control claustrophobia while in the MRI scanner.

Presence of dementia was determined using three sources of information reviewed by a consensus panel of three neurologists and two psychologists. This panel reviewed medical history, physical and neurological exam findings, informant ratings, and mental status measures in order to reach a consensus diagnosis of DS with and without clinical dementia. Informant measures included the Vineland Adaptive Behavior Scales (VABS) [89], Dementia Questionnaire (DMR) [90], and Neuropsychiatric Inventory (NPI) [91]. Three primary cognitive measures were also included in the consensus review and incorporated the Severe Impairment Battery (SIB) [92], Brief Praxis Test (BPT) [93], and modified Fuld Object Memory Examination (FOME) [94]. Following standard clinical criteria for dementia [95, 96] a dementia classification required an informant report of functional decline. The study cohort included 35 adults with DS with 7 participants meeting criteria for dementia (DSAD+) (Table 1).

We also recruited 15 age- and gender-matched (by frequency matching) non-DS control participants (CTL). CTLs reported no history of significant neurologic, cardiovascular, or psychiatric disorders and had no evidence of dementia. All participants

completed informed written consent or assent with guardian consent for the DS participants. The study and research procedures were approved by the University of Kentucky Institutional Review Board.

2.2.2 ASL Methods and Analysis

A three-dimensional (3D) pulsed ASL (PASL) sequence with a gradient and spin echo (GRASE) readout was used for cerebral blood flow (CBF) measurement [53]. The parameters were as follows: TR/TE/TI(inflow time)/TS(saturation time) = 4500/13.04/1900/500 ms, slab thickness = 154 mm, slice-selective labeling gradient = 10mT/m, matrix = 64 x 64 x 44, FOV = 224 x 224 x 154 mm. Nine tagged and untagged data sets were acquired. Five additional M0 images were acquired with no labeling for CBF quantification. DS participants were more likely to move while in the scanner than the control participants, therefore we set a minimum number of non-motion corrupted datasets in order for the participant to be included in the analysis. To be included in the analysis participants were required to have at least 6 tagged and untagged datasets and 3 M0 datasets not corrupted by motion artifact. In cases where more than 6 tagged and untagged datasets were valid, only the first 6 volumes were averaged to maintain a constant expected signal to noise ratio. A total of 10 participants did have at least one dataset excluded, however all participants met the minimum criteria to be included in the analysis.

Selected data sets were co-registered using an intensity-based registration algorithm in Matlab (Mathworks, Natick, MA, USA) before being averaged to yield a tagged, an untagged and an M0 volume for each subject. Quantitative CBF maps (in ml/100g/min) were calculated using in-house Matlab software applying the equation [53],

$$CBF = \frac{6000 \cdot \lambda \cdot (SI_{untag} - SI_{tag}) \cdot e^{\frac{TI}{T_{1,blood}}}}{2 \cdot \alpha \cdot TS \cdot SI_{M0}} \quad (2.1)$$

where λ is the blood-brain partition coefficient (assumed to be 0.9 mL/g) [57], SI_{untag} and SI_{tag} are the average signal intensity of the untagged and tagged volumes respectively, $T_{1,blood}$ is the longitudinal relaxation time of the blood (assumed to be 1.65 seconds at 3.0T) [56], SI_{M0} is the average signal intensity of the M0 volumes, and α is the labeling efficiency (assumed to be 0.98 for PASL) [55].

For CBF analysis, a single ROI encompassing the entire brain volume was drawn manually with the assistance of the in-house Matlab software. This ROI was drawn using the M0 image for its higher contrast to noise ratio and included gray and white matter regions, ventricles, and cerebellum. Global CBF was calculated as the average of all voxels in the ROI

2.2.3 Residual Arterial Signal Scoring

Preliminary observation of the CBF maps revealed that in some subjects a portion of the ASL signal is retained in the large arteries of the brain. In severe cases, the residual arterial signal (RAS) gives the appearance of a low resolution angiogram. An example of minimal, moderate, and severe RAS is shown in Figure 2.1. To quantify the effect of this RAS, two expert reviewers who were blinded to participant information reviewed the same axial slice from each subject to determine if RAS was severe or not. A third blinded reviewer was consulted in the case of disagreement. The Cohen kappa statistic for inter-observer agreement was $\kappa = 0.79$ ($p < 0.001$).

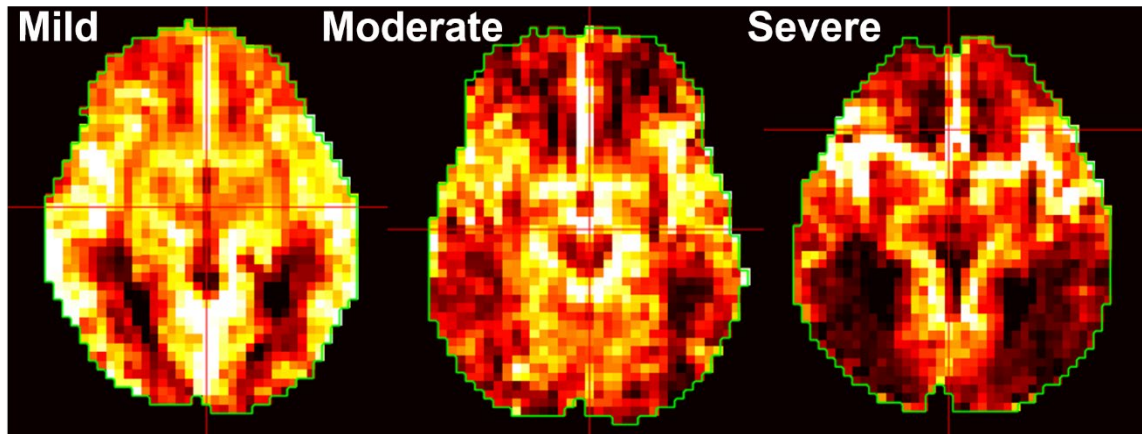


Figure 2.1 Representative CBF maps demonstrating residual arterial signal (RAS)

2.2.4 Statistics

People with DS were separated into an old and young cohort using a Jenks natural breaks optimization [97] such that intra-class variance is minimized. This yielded a discriminating age of 54 years. Participants were also subdivided by DS vs CTL, RAS score (severe or not), and gender. To determine the effect of age group and DS status on global cerebral blood flow, three-way ANOVA was performed while controlling for sex. Tukey's test was used to correct for multiple comparisons, and values of $p < 0.05$ were considered significant. To determine differences in the prevalence of RAS and dementia among age groups and DS status, multi-layered contingency table analysis was performed with post-hoc analysis of standardized residuals.

All statistics are reported as mean \pm standard deviation.

Statistical analysis was performed using Matlab and IBM SPSS Statistics (IBM Corp., Armonk, NY, USA)

2.3 Results

2.3.1 Demographic Characteristics

Table 2.1 displays the demographics and group means on the BPT, SIB, and DMR for the DS groups. Among the 35 adults with DS, 4 females were identified with dementia due to Alzheimer's disease (DSAD). DSAD participants were significantly older ($t(20.39) = -6.74$; $p < 0.001$) had significantly higher scores on DMR ($t(7.04) = -5.99$; $p < 0.001$) compared to DS participants without dementia (referred to as DS). There were no significant differences between DSAD and DS participants on the BPT ($t(4.03) = 0.43$; $p = 0.69$) or SIB ($t(3.96) = 1.48$; $p = 0.21$). Levels of intellectual disability prior to a diagnosis of dementia did not differ between the participants with DS and DSAD (Fisher's exact test $p = 0.45$) as the sample reflected a 50%/50% split of participants in the mild and moderate ranges overall and a 20%/30% split for those persons diagnosed with dementia.

Table 2.1 Demographics

Variable	DS			Control
	DS (n=35)	DSAD+ (n=7)	DSAD- (n=28)	Ctl (n=15)
Female	21 (60.00%)	4 (57.10%)	17 (60.70%)	11 (73.33%)
Age	43.16 (11.12)	56.74 (4.64)	39.77 (9.55)	49.27 (11.64)
BPT	70.50 (7.74)	69.00 (7.44)	70.71 (7.89)	--
SIB	85.13 (11.83)	77.25 (11.35)	86.25 (11.66)	--
DMR	16.38 (16.22)	42.29 (13.83)	9.67 (7.89)	--

2.3.2 Cerebral Blood Flow vs Age

A plot of global CBF versus age reveals a clustering of people with DS over the age of 54 with significantly reduced CBF values (**Fig. 2.2**). This clustering is confirmed by Jenks natural breaks optimization which shows a maximal goodness of variance fit at 54 years. All but one of the DS participants over this age had global CBF values lower than the minimum value of young DS participants. Age group was identified by ANOVA as the strongest contributor to reduced global CBF ($p < 0.001$), and while DS status was not significant as a main effect ($p = 0.09$) the interaction term between age group and DS status was significant ($p = 0.034$). This indicates that the CBF decrease with age is more pronounced among people with DS. Sex was not a significant factor. Post-hoc analysis determined that older people with DS had a significant 31% reduction in CBF (32.3 ± 9.6 mL/100g/min) versus younger people with DS (46.7 ± 6.7 mL/100g/min, $p < 0.001$) (**Fig 2.3**). While CTL subjects over the age of 54 years appeared to also have reduced CBF (40.9 ± 4.1 mL/100g/min) compared to younger controls (45.9 ± 5.8 mL/100g/min), this difference was not significant ($p = 0.59$).

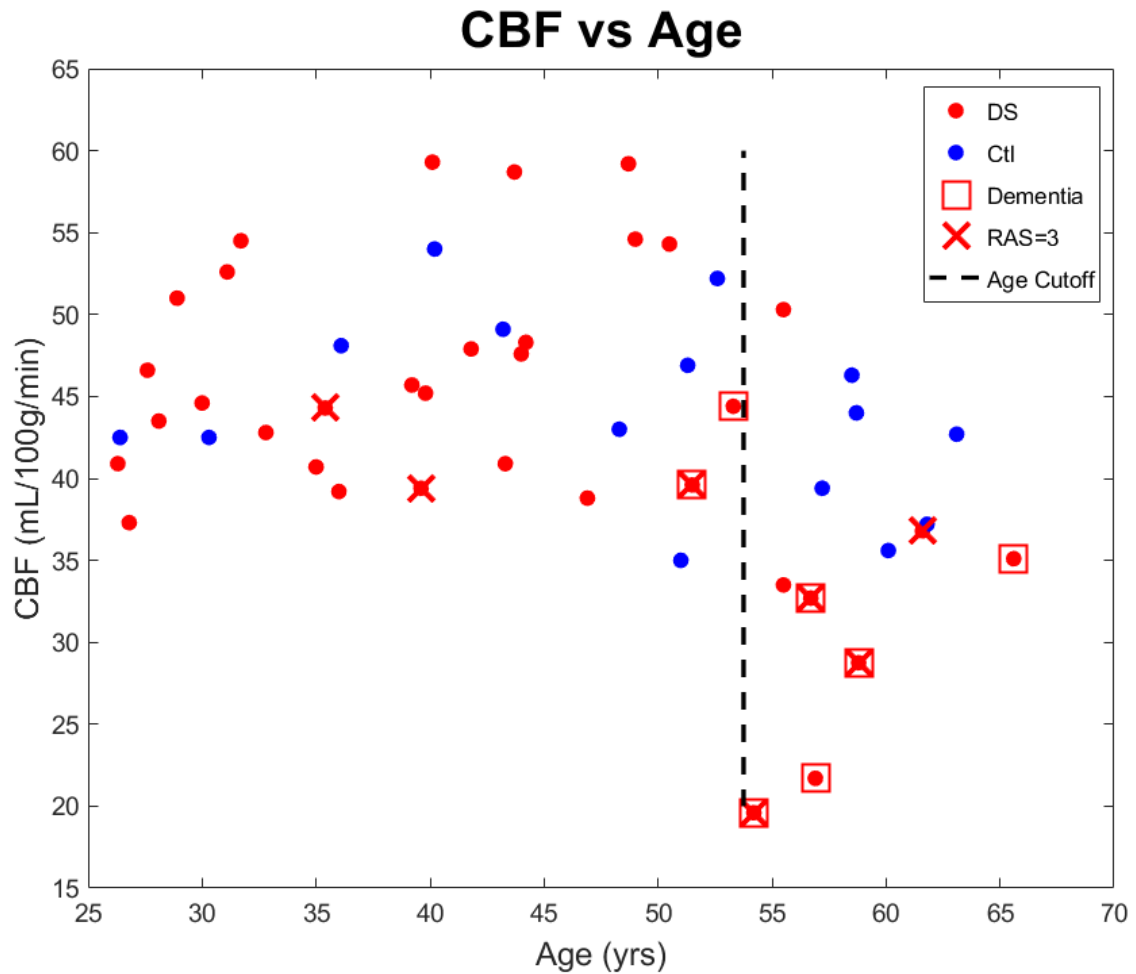


Figure 2.2 Global CBF versus participant age. Participants with severe RAS are indicated with an X, and people with dementia with a square. The dotted line is the Jenks optimized age cutoff for people with DS (54 years), and beyond this age there is a drastic reduction in measured global CBF. The majority of DS participants with dementia as well as a majority of participants with severe RAS lie beyond this line.

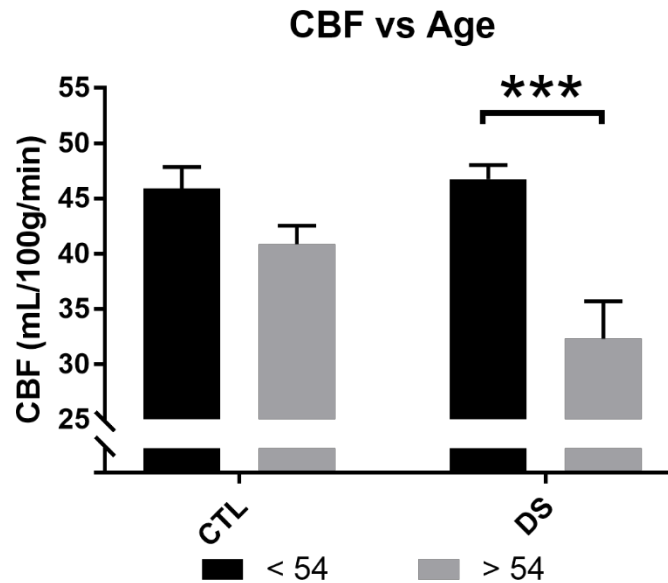


Figure 2.3 Mean global CBF for old (>54) and young (<54) cohorts of DS and CTL participants. No significant difference was observed with age in the CTL participants (>54 = 40.9 ± 4.1 mL/100g/min vs <54 = 45.9 ± 5.8 mL/100g/min, p=0.59), but older DS participants demonstrate a 31% reduction in CBF (32.3 ± 9.6 mL/100g/min) versus younger people with DS (46.7 ± 6.7 mL/100g/min, p <0.001) (***) indicates p<0.001, error bars represent standard error of mean).

2.3.3 Severe RAS and Dementia in People with DS

Pearson chi squared analysis demonstrated dependence between severe RAS score, age group, and DS status ($\chi^2 = 5.83$, p = 0.016). Post-hoc analysis of standardized residuals demonstrates that people with DS over the age of 54 years had a significantly higher proportion of severe RAS scores (50%) vs younger people with DS (11%) or non-DS controls (0%) (p = 0.0078). Similar dependence was shown between dementia status, age group, and DS status ($\chi^2 = 11.7$, p < 0.001), and post-hoc analysis showed a much higher prevalence of dementia in older people with DS (63%) than younger people with DS (7%) or non-DS controls (0%, p < 0.001).

2.4 Discussion

In this study we report a reduction in global CBF as measured by PASL in older people with DS. There are two underlying mechanisms that could account for this reduction, and both are likely contributors to our measurement. First, the reduced measured blood flow may be a true reduction in perfusion in older DS brain tissue compared to young DS and non-DS controls. Second, the lower measured CBF may be exaggerated by the sensitivity of the ASL technique to prolonged arterial transit times that manifest as RAS.

Our measured CBF reduction in old versus young people with DS may represent a true reduction in perfusion. This is supported in the literature by a case study by Purdi, et al, in 1994 that described a marked decrease in cortical blood flow in a 52 year old person with DS (Purdi, et al., 1994). Another 2017 doppler study of 6 people with DS compared to 7 age matched controls showed a 30% reduction in carotid blood flow and a 20% reduction in vascular conductance (Wee, et. al., 2017). CAA can lead to micro and macro hemorrhages [98], and brain A β 40 (typically associated with CAA) rises exponentially with age in DS [99]. CAA also affects older people with DS to a greater extent than in sporadic AD [85]. Thus we conclude that one mechanism responsible for the observed reduction in global CBF is, in fact, due to reduced perfusion in older people with DS.

A portion of the perfusion reduction may also be due to delayed arterial perfusion as indicated by severe RAS. Half of the older people with DS and 11% of younger people with DS in this comparison displayed severe RAS signs. The 3D GRASE readout of our PASL sequence is known to suppress the signal intensity of faster moving arterial blood with the rapid and repeated application of gradients similar to the signal suppression observed in diffusion weighted imaging [87]. Therefore, extreme delays in perfusion can

cause the blood bolus to remain in the large arteries and lead to an apparent suppression of the measured signal intensity. This causes an underestimate of the true CBF. Zaharchuk et al., 2009, observed a similarly low CBF in the watershed regions, last to perfuse, as measured by ASL in 18 out of 139 (13%) subjects using ASL when compared to normal bolus delivered perfusion MRI [100]. Our inflow time of 1900ms should be less sensitive to RAS than the 1500ms used by Zaharchuk et al., and the average age of the subjects that showed reduced CBF in that study was 71 yrs. Yet we have observed this phenomenon in 4 out of 8 (50%) of our DS participants between the ages of 54-65 yrs. Though we are unable to quantify the ATT with only a single inflow time, it appears that ATT is delayed in DS compared with the CTL cohort based on the prevalence and severity of RAS. There is a significant increase in severe RAS after the age of 54 years, and this delay is partially responsible for our decreased CBF measurements in old versus young people with DS. This is consistent with research demonstrating a 30% lower arterial conductance in DS in the carotid arteries (18-40yrs) [101], a 15% increase in carotid stiffness in young DS vs nonDS [102], and a carotid-femoral pulse wave velocity that decreases faster with age in DS than nonDS (although this effect is not significant after a systolic blood pressure adjustment) [103]. Thus, even though this second possible mechanism is not a direct measure of reduced perfusion, it is still likely an indicator of changes in the cerebrovasculature.

Higher blood flow velocities could be a result of stenosis due to atherosclerosis. However, given that our DS volunteers typically do not have atherosclerosis or hypertension, it is unlikely that this is an underlying factor for DS. It is more likely that

CAA may be contributing to the perfusion deficit by affecting blood vessels ability to dilate and constrict, whether mechanically or through autonomic dysregulation.

The current study also provides some insight on the role of cerebrovascular dysfunction in DS. Previous imaging studies show the effects of vascular deficits on white matter (WM) in DS. An interesting observation from our first WM integrity studies using diffusion tensor imaging (DTI) was that there is a periventricular distribution of WM integrity losses, and this is a region that typically shows white matter hyperintensities (WMH) in sporadic AD [104]. WMH volume, particularly in parietal regions, is elevated among individuals with and at risk for AD, predicts future diagnosis of AD, and predicts the rate of progression of cognitive symptoms among individuals with AD [105]. Further, previous studies show that ex vivo imaging of autopsy brain indicates an overlap between fractional anisotropy (FA) in DTI studies and WMH that reflect vascular deficits [106], and WMH prominent in periventricular regions lead to reduced FA [107]. However, these studies do not capture the progression of vascular dysfunction with age, particularly as it relates the onset of dementia.

Virtually all DS adults have sufficient neuropathology for a diagnosis of AD by 40 years [108-110], including senile plaques (SP-beta-amyloid ($A\beta$) protein) and neurofibrillary tangles (hyperphosphorylated tau protein). This is largely due to the third copy of chromosome 21 in DS because $A\beta$ is derived from the β -amyloid precursor protein (APP) on chromosome 21 [111]. $A\beta$ accumulation in diffuse plaques does not begin systematically until after the age of 30 years [108]. Between the ages of 30 and 40 years, neuropathology accumulates until it reaches levels sufficient for AD [110].

What was previously unknown was whether this accumulation of A β was accompanied by vascular dysfunction in DS. This is particularly relevant because of the increasing evidence of the role of CVD in the development and progression of sporadic AD. In late onset AD, reduced CBF precedes the transition to dementia by decades [112], and mixed etiology dementia is very common [65]. In this study, by contrast, we do not observe a reduction in measured CBF among people with DS until the middle of the 6th decade, corresponding to the typical age of onset for dementia in this population. This suggests that the protective vascular profile (absence of atheroma and reduced blood pressure) of DS may work to delay the progression of AD until it is overwhelmed by amyloidopathy. Supporting this hypothesis are data showing the impact of amyloid on endothelial cell function [113].

In a previous study of 70 adults with DS ranging in age from 40-66 years, there was an absence of atheroma and lower blood pressure than similarly aged adults without DS [77]. Other studies also report low frequencies of atherosclerosis and arteriolosclerosis [78, 79, 85].

While these common signs of CVD are rare in DS, CAA is consistently observed in older individuals with DS >55 yrs [82-84]. CAA is the common term used to define the deposition of amyloid in the walls of medium- and small-size leptomeningeal and cortical arteries, arterioles and, less frequently, capillaries and veins. These depositions contain post-translationally modified A β [114] and can lead to micro and macro hemorrhages [98]. Importantly, people with DS show more extensive and severe CAA than older people with sporadic AD [85]. Furthermore, the same study shows that the transition to severe CAA in DS occurs in the sixth decade [85] around the same age as the drop in global CBF observed

in this study. Interestingly, there are reports that CAA in DS is associated with extensive hemorrhages in some studies (Belza and Urich, 1986; Donahue et al., 1998; McCarron et al., 1998; Mendel et al., 2010; Naito et al., 2008) but not in others [82, 83]. Buss and colleagues discuss in their review whether people with DS are protected from strokes [115]. Micro and macro hemorrhages that result from CAA typically manifest as WMH, and preliminary data from our study shows that by SWI, we can identify hypointensities consistent with CAA, and we have published data showing that brain A β 40 (typically associated with CAA) rises exponentially with age in DS [99].

Future longitudinal studies involving this cohort will be important to establish the sequence of CAA and perfusion deficits. Also, our study included only one inflow time and was therefore unable to calculate ATT, future studies with multiple inflow times would be able to generate maps of ATT to better investigate the change in vascular delivery occurring with age in DS. While we observed some interesting regional patterns, namely a more pronounced deficit in parieto-occipital regions of patients with severe RAS, we were not able to acquire specific regional volumes of interest for analysis. Regional analysis is particularly difficult in this population due to a lack of a standard atlas for the DS brain. Furthermore, motion artifacts are common in high resolution anatomical images when scanning people with DS. This makes coregistration and automatic segmentation extremely challenging, and manual regional segmentation was not feasible at this time.

There have been few studies investigating the role of CVD on aging, cognition and dementia in DS. Based upon autopsy studies, there should be significant CVD that could be captured and quantified by the appropriate MR imaging protocols. In terms of designing future clinical trials, characterizing the age of onset and extent of CVD in adults with DS

will be critical given that CVD is mediated to large extent by lifestyle factors that are amenable to intervention.

CHAPTER 3. NOVEL CALIBRATED SHORT TR RECOVERY (CASTRR) METHOD FOR BRAIN-BLOOD PARTITION COEFFICIENT CORRECTION IN MICE

3.1 Introduction

Arterial spin labeling (ASL) is a non-invasive, quantitative magnetic resonance imaging (MRI) technique used to measure cerebral blood flow (CBF) in a wide variety of human conditions. A growing number of studies are using ASL to measure perfusion in a variety of preclinical murine models including, aging [116, 117], Alzheimer's disease [47, 118, 119], ischemic injury [50, 120, 121], traumatic brain injury [48], and vascular dementia [49]. This technique is based on using magnetically labeled protons on water molecules in the blood as a tracer substance to measure perfusion. As in other tracer-based techniques, in order to accurately quantify perfusion it is necessary to determine the partition coefficient of the tracer, which is in this case the relative solubility of water in the brain tissue vs the blood. The brain-blood partition coefficient (BBPC) is tissue-specific and varies with age, species, pathology, and particularly with brain region [57, 60-62]. Thus the BBPC must be measured directly, and while MRI is well suited to measure water content in the brain, the current techniques to do so have prohibitively long acquisition times [58, 62]. Because of this, it is standard practice in ASL quantification to assume a BBPC value of 0.9 mL/g based on desiccation experiments performed on ex-vivo human brain tissue [53, 57]. This global average value is used for all regions of the brain, all ages and pathologies, and is even adopted when performing ASL in mice [122-125].

Previous studies have determined a wide range of BBPC values in the human brain, particularly between relatively lipophilic white matter (0.82mL/g) and hydrophilic gray matter (0.99mL/g) [57, 59, 126]. Yet even among gray matter regions the BBPC can vary

as much as 20% [59]. Measurements in non-human primates have demonstrated lower BBPC values than humans with an even greater regional variability [61]. An MRI study of BBPC in mice reported an average BBPC of 0.89mL/g with little regional variability among gray matter regions of interest, but no white matter BBPC values were reported [62]. Because ASL has inherently low signal-to-noise ratio and the resolution requirements of scanning mouse brains are particularly high, it is necessary that the quantification methods introduce as little error as possible. Failure to correct for intra-subject regional variability as well as inter-subject variability in BBPC may result in a loss of sensitivity to perfusion deficits when using ASL. This is especially true when studying white matter regions which have both lower perfusion and lower BBPC.

In this study, we used a calibrated short TR recovery (CaSTRR) MRI sequence to measure proton density. This protocol is similar to one used previously by Leithner et al. to measure BBPC in mice [62], but has been modified to greatly reduce the acquisition time. Proton density was determined for the brain tissue as well as a fresh sample of each mouse's blood placed adjacent to the animal's head in order to calculate BBPC. Then cerebral perfusion was measured using a pseudo-continuous ASL (pCASL) technique to compare CBF maps that were uncorrected to maps that were corrected for regional BBPC. Particular attention was given to the white matter region of interest in the corpus callosum.

3.2 Methods

3.2.1 Animal Model

All animal experiments were performed in accordance with NIH guidelines and approved by the University of Kentucky Institutional Animal Care and Use Committee

(Approval number #2014-1264). Male C57Bl/6N mice aged 12 months (n=8) were acquired from the National Institute of Aging colony. MRI experiments were performed using a 7T MR scanner (Clinscan, Brüker BioSpin, Germany) at the MRI and Spectroscopy Center at the University of Kentucky. Mice were anesthetized using a 4% mixture of isoflurane with air for induction and then maintained using 1.2% isoflurane such that the respiration rate was kept within 50-80 breaths/min. Rectal temperature was also monitored continually and maintained at $37 \pm 1^\circ\text{C}$ using a water-heated bed.

While under anesthesia a fresh blood sample was taken from the facial vein and sealed in a glass capillary tube with ethylenediaminetetraacetate (EDTA) as an anticoagulant. This sample was then placed adjacent to the head of the mouse in order to measure the proton density of the blood (**Fig. 3.1-A**).

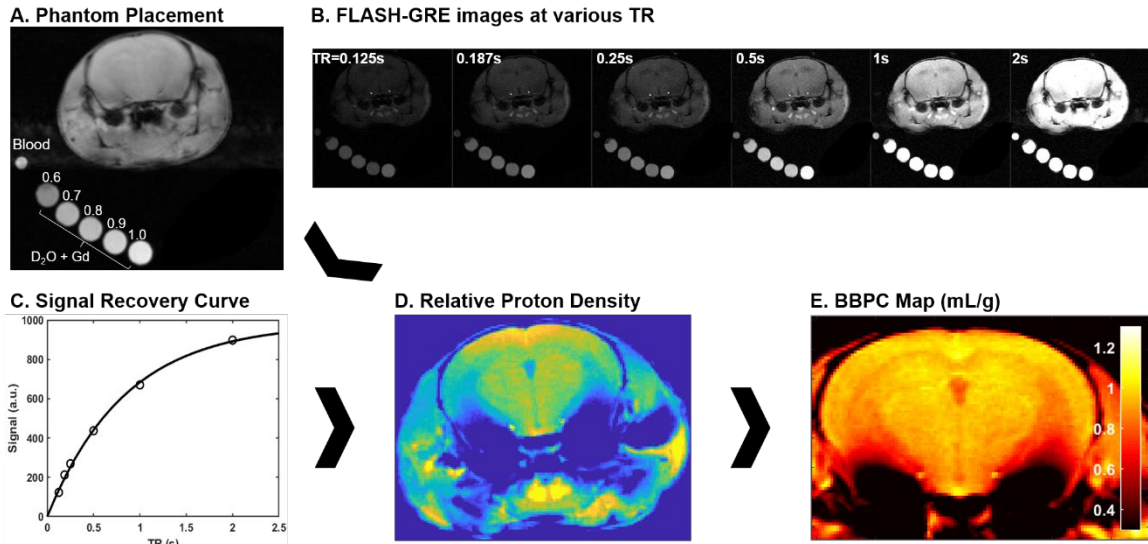


Figure 3.1 Explanation of the calibrated short repetition time recovery (CaSTRR) imaging protocol to measure BBPC. (A) One CaSTRR acquisition showing the placement of blood and gadolinium doped phantoms in relation to the head of the mouse. (B) A representative series of FLASH-GRE images used for the CaSTRR method. (C) A representative signal recovery curve from a single voxel of brain tissue located in the cortex region of interest (circles) along with the exponential regression used to estimate the relative proton density of the voxel (line). (D) A representative map of relative proton density derived from the voxel-wise signal recovery curves. (E) The final BBPC map calculated as the ratio of proton density in the brain to the average proton density of the blood phantom and corrected for the density of brain tissue.

3.2.2 Calibrated Short TR Recovery Imaging Protocol

Both CaSTRR and pCASL images were acquired consecutively in a single imaging session. Because the CaSTRR acquisitions and the pCASL acquisitions require different receiver coils, a custom 3-D printed nose was developed to accommodate both a birdcage style volume coil and a phased-array surface coil so that the coils could be changed without disturbing the orientation of the mouse. This nose cone also facilitated the placement of phantoms adjacent to the head of the mouse.

Mice were scanned with a series of five phantoms placed alongside their head in the scanner (**Fig. 3.1-A**). The phantoms contained a mixture of deuterium oxide with

distilled water such that the water contents of the phantoms were 60, 70, 80, 90 and 100% distilled water [62]. The phantoms were also doped with 0.07mM gadobutrol (Gadavist, Bayer Healthcare Pharmaceuticals, Whippany NJ, USA) such that the longitudinal relaxation rate (T1) was similar to the T1 of brain tissue (~1.6s at 7T) [127].

The CaSTRR proton density measurements were acquired using a 39mm birdcage transmit/receive coil to ensure the most uniform coil sensitivity profile possible. To measure the proton density a series of image stacks was acquired using a phase-spoiled, fast low-angle shot gradient echo (FLASH-GRE) sequence with varying repetition times (TR = 125, 187, 250, 500, 1000, 2000 ms) (**Fig. 3.1-B**). The shortest possible echo time (TE = 3.2 ms) was used to minimize T2* decay. In order to improve signal to noise, multiple averages were taken for the images with TR = 125 ms (4 averages), 187 ms (4 averages) and 250 ms (2 averages). Image matrix parameters were as follows: field of view = 2.8 cm x 2.8 cm, matrix = 256 x 256, in-plane resolution = 0.11 mm x 0.11 mm, slice thickness = 1mm, number of slices = 10, flip angle = 90°, acquisition time = 17 minutes [62].

BBPC maps were calculated in a voxel-wise manner by first fitting the signal recovery curve (**Fig. 3.1-C**) to the mono-exponential equation $S = M_0 * [1 - e^{-(TR/T_1)}]$ to yield a map of M_0 (**Fig 3.1-D**). Next the M_0 map was normalized to the respective phantom series by fitting a linear regression to the average M_0 value in each phantom. Finally, the proton density in each voxel of the brain was compared to the average proton density of the blood ROI using the equation $BBPC = M_{0,brain} / (M_{0,blood} * 1.04g/mL)$ (**Fig. 3.1-E**) [58, 62].

3.2.3 Pseudo-Continuous ASL Protocol

For pCASL acquisitions, paired control and label images were acquired using a four-channel phased-array surface receive coil for increased signal to noise, and a whole body volume transmit coil to improve the tagging efficiency of the blood [119]. Image pairs were acquired in an interleaved fashion with a train of Hanning window-shaped radiofrequency pulses of duration/spacing = 200/200 μ s, flip angle = 25° and slice-selective gradient = 9 mT/m, and a labeling duration = 2100 ms. The images were acquired by 2D multi-slice spin-echo single shot echo planar imaging with FOV = 1.8 cm x 1.3 cm, matrix = 128 \times 96, in-plane resolution = 0.14 mm x 0.14 mm, slice thickness = 1 mm, 6 slices, TE/TR = 20/4000ms, label duration = 1600ms, post-label delay = 0s, and averages = 120. A separate, unlabeled acquisition with TR = 10s and averages = 6 was used to normalize for the receiver coil profile. Total acquisition time for pCASL was 9 minutes.

When analyzing the CBF maps, the two centermost slices containing the hippocampus were selected for analysis. The brain regions of the CaSTRR and pCASL images were isolated independently using an automated skull-stripping algorithm and then coregistered using an intensity based registration algorithm. The quantitative CBF maps were calculated from the pCASL images according to the equation [53]

$$CBF(mL/g/min) = \frac{60 * BBPC * e^{\left(\frac{PLD}{T_{1,blood}}\right)}}{2 * \alpha * \left(1 - e^{\left(\frac{LD}{T_{1,blood}}\right)}\right)} * \frac{C_{tl} - L_{bl}}{M_0}, \quad (3.1)$$

where PLD is post-label delay, LD is label duration, $T_{1,blood}$ is the longitudinal relaxation of blood (2.2s at 7T), and α is label efficiency (0.85) [53]. For standard CBF maps the

BBPC was assumed to be a constant 0.9mL/g. Then a corrected CBF map was calculated by using the CaSTRR derived BBPC maps in place of the assumed constant.

3.2.4 Image Analysis

Regions of interest encompassing the superior neocortex, corpus callosum, and hippocampus were drawn manually on each analyzed slice. BBPC, uncorrected CBF, and corrected CBF values were averaged for each region of interest. Gray-white contrast was determined for each slice as the absolute difference of average CBF values in gray and white matter regions of interest. All analysis was performed with in-house written scripts in Matlab (Mathworks, Natick, MA, USA).

3.2.5 Statistics

Statistical analysis was performed using SPSS (IBM, Armonk, New York, USA). All data are expressed as mean \pm standard deviation. Group comparisons were assessed using one- and two-way analysis of variance with Tukey's post-hoc test. Values of $p < 0.05$ were considered statistically significant.

3.3 Results

3.3.1 Corpus Callosum Demonstrates Reduced BBPC Compared To Neocortex

The average BBPC values in the neocortex, corpus callosum, and the hippocampus were determined for each mouse and the average of all mice is reported in Table 1. The highest BBPC value was observed in the neocortex ($\mu_{\text{Ctx}} = 0.99 \pm 0.04$ mL/g) which was

significantly higher than the corpus callosum ($\mu_{CC} = 0.93 \pm 0.05$ mL/g, $p = 0.035$), and also higher than the hippocampus, though not significantly ($\mu_{HC} = 0.95 \pm 0.4$ mL/g, $p = 0.17$) (Figs. 3.2 & 3.3).

Table 3.1 Mean Partition Coefficient and Perfusion Values by Region

Regional Values	Neocortex	Hippocampus	Corpus Callosum
BBPC (mL/g)	$0.99 \pm .04$	0.95 ± 0.04	0.93 ± 0.05
CBF, uncorrected (mL/g/min)	2.81 ± 0.4	2.90 ± 0.6	1.44 ± 0.3
CBF, corrected (mL/g/min)	3.09 ± 0.5	3.07 ± 0.7	1.51 ± 0.4
Gray-White Perfusion Contrast	Neocortex vs Corpus	Hippocampus vs Corpus	
$\Delta CBF_{\text{Uncorrected}}$ (mL/g/min)	1.39 ± 0.4	1.46 ± 0.4	
$\Delta CBF_{\text{Corrected}}$ (mL/g/min)	1.59 ± 0.5	1.54 ± 0.4	
Contrast improvement (% , 95% CI)	14.2%, 9.6-18.8%	5.8%, 1.4-10.1%	

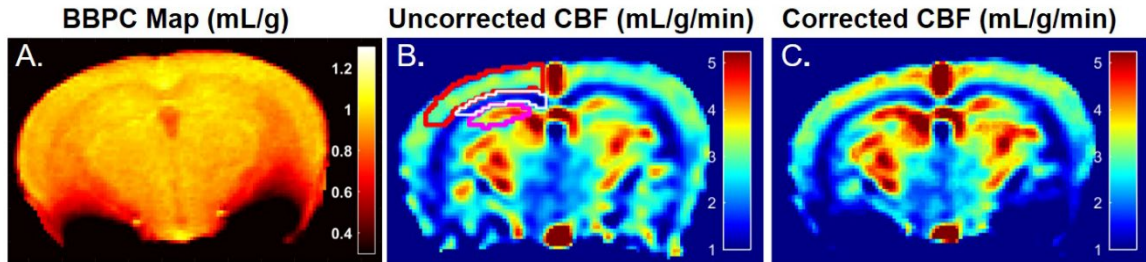


Figure 3.2 Representative maps of BBPC and CBF. Maps of BBPC (A) demonstrates elevated BBPC in the neocortex relative to the corpus callosum and hippocampus ($\mu_{Ctx}= 0.99 \pm 0.04\text{mL/g}$, $\mu_{CC}= 0.93 \pm 0.05\text{mL/g}$, $\mu_{Hc}= 0.95 \pm 0.04\text{mL/g}$). Maps of the uncorrected (B) and BBPC-corrected (C) cerebral blood flow demonstrate the improved contrast between gray matter in the neocortex (top) and hippocampus (bottom) and the white matter in the corpus callosum (middle). While only one side is shown, regions of interest were drawn bilaterally and applied equally to all three maps.

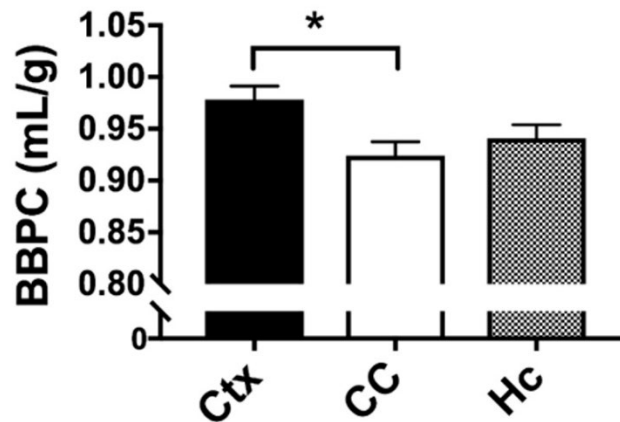


Figure 3.3 Regional analysis of BBPC demonstrates significantly higher BBPC in the neocortex relative to the corpus callosum ($\mu_{Ctx}= 0.99 \pm 0.04\text{mL/g}$, $\mu_{CC}= 0.93 \pm 0.05\text{mL/g}$, $p = 0.035$), while the hippocampus had a BBPC of $\mu_{Hc}= 0.95 \pm 0.04\text{mL/g}$.

3.3.2 Corpus Callosum Demonstrates Lower Perfusion than Gray Matter

Elevated perfusion in gray matter regions was observed relative to the corpus callosum in both uncorrected CBF maps and maps with voxel-wise BBPC correction (Fig. 3.4). In the uncorrected maps the hippocampus demonstrated the greatest perfusion ($2.90 \pm 0.6 \text{ mL/g/min}$) followed by the neocortex ($2.81 \pm 0.4 \text{ mL/g/min}$) with significantly less perfusion in the corpus callosum ($1.44 \pm 0.3 \text{ mL/g/min}$, $p < 0.001$). However, when the maps

were corrected for BBPC the perfusion in the neocortex was highest (3.09 ± 0.5 mL/g/min) followed by the hippocampus (3.07 ± 0.7 mL/g/min) with significantly less perfusion again in the corpus callosum (1.51 ± 0.4 mL/g/min, $p < 0.001$). None of the regions demonstrated significant changes in average CBF values due to BBPC correction (corrected vs uncorrected CBF, $p_{\text{Ctx}} = 0.31$, $p_{\text{CC}} = 0.66$, $p_{\text{HC}} = 0.61$).

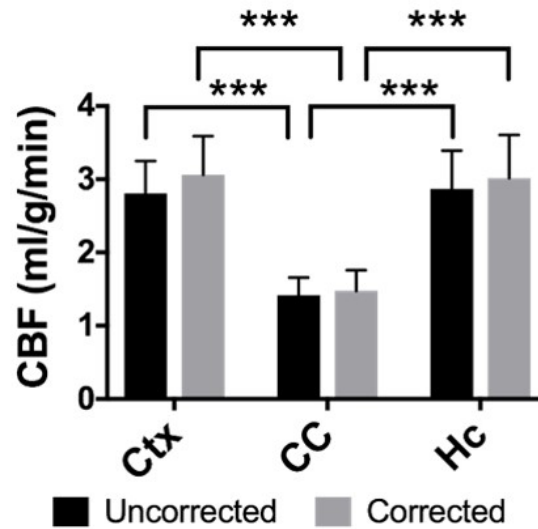


Figure 3.4 CBF by Region The gray matter regions of the neocortex ($\mu_{\text{uncorrected}} = 2.81 \pm 0.4$ mL/g/min, $\mu_{\text{corrected}} = 3.09 \pm 0.5$ mL/g/min) and hippocampus ($\mu_{\text{uncorrected}} = 2.90 \pm 0.6$ mL/g/min, $\mu_{\text{corrected}} = 3.07 \pm 0.7$ mL/g/min) demonstrate significantly higher cerebral blood flow than the white matter corpus callosum ($\mu_{\text{uncorrected}} = 1.44 \pm 0.3$ mL/g/min, $\mu_{\text{corrected}} = 1.51 \pm 0.4$ mL/g/min) in both the uncorrected and BBPC-corrected CBF maps. (***) indicates $p < 0.001$).

3.3.3 Corrected CBF Maps Demonstrate Greater Contrast than Uncorrected

When perfusion in gray matter regions is compared to the white matter of the corpus callosum for each mouse, the average difference in perfusion for the neocortex is 1.39 ± 0.4 mL/g/min in the uncorrected maps, but it is 1.59 ± 0.5 mL/g/min in the BBPC corrected maps, this constitutes a 14.2% increase in contrast between these regions (95% CI = 9.6-18.8%). For the hippocampus the difference in perfusion is 1.46 ± 0.4 mL/g/min in the

uncorrected maps and 1.54 ± 0.4 mL/g/min in the corrected maps, or a 5.8% improvement (95% CI = 1.4%-10.1%) (Fig. 3.5 and Table 1).

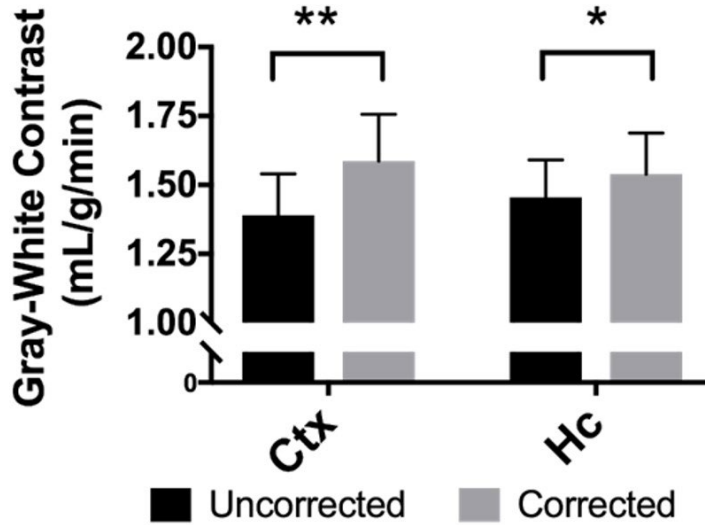


Figure 3.5 Improved contrast from BBPC correction. Contrast between the neocortex and corpus callosum was improved by 14.2% (95% CI= 9.6-18.8%, $\Delta\text{CBF}_{\text{uncorrected}} = 1.39 \pm 0.4\text{mL/g/min}$, $\Delta\text{CBF}_{\text{corrected}} = 1.59 \pm 0.5$ mL/g/min) and between the hippocampus and corpus callosum by 5.8% (95% CI= 1.4-10.1%, $\Delta\text{CBF}_{\text{uncorrected}} = 1.46 \pm 0.4\text{mL/g/min}$, $\Delta\text{CBF}_{\text{corrected}} = 1.54 \pm 0.4\text{mL/g/min}$). (* indicates $p < 0.05$, ** indicates $p < 0.01$).

3.4 Discussion

Using CaSTRR imaging we were able to produce high quality BBPC maps suitable for voxel-wise correction of perfusion measurements much faster than previous demonstrated. We determined that the average BBPC in the neocortex was 0.99 ± 0.04 mL/g and in the hippocampus the BBPC was 0.95 ± 0.4 mL/g. We also determined the BBPC in the white matter structure of the corpus callosum to be 0.93 ± 0.05 mL/g which has not previously been reported in mice. We also found significantly lower CBF in the corpus callosum than the neocortex and the hippocampus. Finally, when CBF maps were corrected for regional variability in BBPC the gray-white matter contrast was improved by as much as 14%.

The significant reduction in the acquisition time of BBPC maps to only 17 minutes increases the feasibility of including such a scan during an ASL protocol. We were also able to perform a voxel-wise correction due in part to the custom nose cone designed to immobilize the mouse's head while receiver coils are changed. The result of this correction is improved sensitivity to regional perfusion differences in CBF. This study acquired high resolution BBPC maps as was done in previous studies, but those maps had to be down-sampled by 22% to match the resolution of the pCASL acquisition when calculating CBF. This means that further gains could be made in either acquisition time or signal to noise ratio by acquiring CaSTRR images at the same resolution as the ASL image. Furthermore, since the original BBPC mapping technique was adapted to use in mice from a previously established technique in humans, CaSTRR imaging should be rapidly translatable back to the clinical setting [58]. In fact, a recently published study on healthy human volunteers demonstrated that an alternative method of correcting CBF maps for BBPC variability also resulted in increased contrast between gray and white matter [128]. This is consistent with our study and highlights the potential benefit of BBPC correction.

The improved regional specificity of CBF maps that are corrected for BBPC variability will be particularly relevant in the study of white matter pathologies [129]. There is growing interest in vascular dysfunctions that accompany commonly observed white matter pathologies like multiple sclerosis [130, 131], white matter hyperintensities [132], and schizophrenia [133]. The inherently low signal to noise of ASL is exacerbated in white matter where there is far less perfusion than gray matter. This means differences in perfusion will be even more subtle and could be confounded by changes in BBPC. While adding a second measurement to the CBF calculation with its inherent noise may introduce

more variability in the CBF maps, the ability to account for significant differences in BBPC may increase sensitivity when comparing groups or regions with small perfusion differences.

It should be noted that the CaSTRR technique differs from the one described by Leithner et al. in a few key aspects. The primary difference is the choice to use logarithmically spaced TRs and omit TRs longer than 2 seconds. This change reduced the acquisition time by 87% from ~130 minutes [62] to 17 minutes. In previously published BBPC results, phantoms consisted of pure H₂O/D₂O solutions with very long T₁ recovery times which necessitated long TRs [58, 62]. By adding gadolinium to the water phantoms we were able to reduce the T₁ of the phantoms to approximately match the tissue thereby obviating the long TR scans that accounted for the vast majority of scan time. It should also be noted that Leithner et al. used 8-16 week old 129S6/SvEv mice. We would expect younger mice to have a higher BBPC than the 12 month old mice used in our experiment, however we observed higher BBPC values in our C57Bl/6N mice than were reported by Leithner et al. Future studies will need to consider the possibility that BBPC could vary with genetic strain.

There are several limitations to this study. While previous studies have used a uniform phantom to try and correct for the field inhomogeneity, variations were typically less than 5% and it is unlikely that the B1 field will be the same in a uniform phantom as it is while scanning a mouse [58, 62]. For this reason we chose not to perform any post-hoc field correction and instead assumed a uniform field and receiver profile. More advanced field correction techniques may be useful. Also this study did not include a comparison to a post-mortem desiccation experiment. The standard BBPC mapping

technique has been shown to underestimate the BBPC when compared to desiccation because a small fraction of water in the brain tissue does not contribute to the MRI signal [62]. Thus the overestimation of BBPC by CaSTRR may compensate for this effect, though not because it is more sensitive to this hidden water. Furthermore, regional analysis is not possible with desiccation, so desiccation could not confirm the regional differences observed by CaSTRR imaging. Finally there are two potential mechanisms for signal loss due to the gradient echo readout used to acquire CaSTRR images. The first is rapid T_2^* decay, and while this study attempts to minimize this effect by using the shortest possible echo time, a multi-echo acquisition would allow for a more complete compensation. The second is sensitivity to susceptibility artifacts at air-tissue interfaces. This can be seen as a signal loss adjacent to the ear canals, and in this study we were forced to examine only those superior regions of the brain that were not affected by this artifact. For studies involving deep brain structures it may be necessary to separately acquire a B1 field map to correct for susceptibility variation.

In conclusion, the CaSTRR method produced maps of BBPC in mice with quality comparable to the current standard method while requiring far less acquisition time. This enables voxel-wise, empirical correction of CBF maps for regional and inter-subject variability in BBPC. These corrected CBF maps demonstrate improved contrast between gray and white matter regions. With growing interest in using ASL to measure white matter perfusion, this technique may have considerable value in studying pre-clinical models of white matter pathologies as well as potential for rapid translation to use in human studies.

CHAPTER 4. BRAIN-BLOOD PARTITION COEFFICIENT AND CEREBRAL BLOOD FLOW IN CANINES USING CALIBRATED SHORT TR RECOVERY (CASTRR) CORRECTION METHOD

4.1 Introduction

When using tracer-based techniques like arterial spin labeling (ASL) to quantify cerebral blood flow (CBF), it is necessary to determine the partition coefficient of the tracer between the perfused tissue and the arterial blood. ASL is a non-invasive, quantitative magnetic resonance imaging (MRI) technique that uses magnetically labeled protons in the water molecules of the blood as the tracer [25, 53, 87]. So in the case of ASL, the relevant partition coefficient is the brain-blood partition coefficient of water (BBPC) which is the ratio of the solubility of water in brain tissue to the solubility of water in the blood. The BBPC is tissue specific and varies with age, species, pathology, and brain region [57, 60-62]. This means that BBPC should be determined experimentally for each subject.

However, the standard practice in ASL studies is to assume a constant BBPC value of 0.9mL/g for all regions of the brain regardless of the known variability of this parameter [53, 57]. This assumption is made because the previously published MRI methods to experimentally determine BBPC required prohibitively long acquisition times and ASL studies were generally focused on gray matter perfusion where BBPC variability was assumed to be small [58, 62]. A recent study in mice at 7T reported an 87% reduction in the acquisition time for BBPC maps using an MRI technique called calibrated short TR recovery (CaSTRR) [134]. Like previous methods, CaSTRR determines relative proton density using a series of gradient echo acquisitions with varying repetition times (TR) and then calibrates the proton density map using a set of deuterium doped phantoms which provide an absolute scale of water content. The method is accelerated in CaSTRR by using

shorter TR values and using gadolinium doped water phantoms to acquire similar quality BBPC maps in a fraction of the time.

The goal of this study is to apply the CaSTRR technique to a cohort of healthy canines using a protocol suited for application in humans at 3T. To do so we acquired BBPC images using a CaSTRR protocol adapted for use on a 3T human scanner. We then acquired CBF maps using pseudo-continuous ASL (pCASL) to assess the effect of BBPC correction on CBF maps, and high resolution anatomical images using magnetization prepared rapid acquisition gradient echo (MPRAGE) to facilitate segmentation and coregistration. Finally, we compare two methods of normalizing the proton density maps using the doped water phantoms and using blood water content derived from hematocrit values.

4.2 Methods

4.2.1 Animal Model

All animal experiments were performed in accordance with NIH guidelines and approved by the University of Kentucky Institutional Animal Care and Use Committee (approval number #2017-2680). Middle aged beagles (n=17, age = 5.0-8.0 yrs, male = 24%) were acquired as part of a longitudinal study on aging and Alzheimer's disease. The scans in this report represent pretreatment observations, and all animals were healthy at the time of their scans. The animals were anesthetized during the MRI procedure using 3-4 mg/Kg propofol for induction and 1-4% isoflurane mixed with air for maintenance. Respiratory rate, heart rate, body temperature, and blood pressure were monitored and maintained throughout the procedure. Two 5 mL vials of blood were drawn from the

jugular vein using ethylenediaminetetraacetate (EDTA) treated vials. One of these was placed in the scanner with the animal according to the CaSTRR protocol, and the other was sent for laboratory analysis including hematocrit (ANTECH Diagnostics, Louisville, KY, USA).

4.2.2 Scanning procedure

MRI experiments were performed using a 3T Siemens Trio scanner (Siemens, Erlangen, Germany) at the MRI and Spectroscopy Center at the University of Kentucky. The animal was placed prone with the head resting in a 155 mm diameter, 15 channel transmit/receive birdcage coil commonly used for scanning human knees. The doped water phantoms along with blood sample were centered on the top of the head. The CaSTRR, pCASL, and MPRAGE acquisitions were all acquired in a single scanning session.

4.2.3 Calibrated Short TR Recovery Imaging

For the CaSTRR proton density measurements a series of 2-D image stacks were acquired using a phase-spoiled, fast low-angle shot gradient echo (FLASH-GRE) sequence with varying repetition times (TR = 125, 250, 500, 1000, 2000 ms) [134]. The shortest possible echo time (TE = 1.9 ms) was used to minimize T2* decay. Image matrix parameters were: field of view = 135 x 124 mm, matrix = 96 x 88, in-plane resolution = 1.4 x 1.4 mm, slice thickness = 3 mm, number of slices = 30, flip angle = 90°, acquisition time = 4 minutes. (**Fig. 4.1-A**)

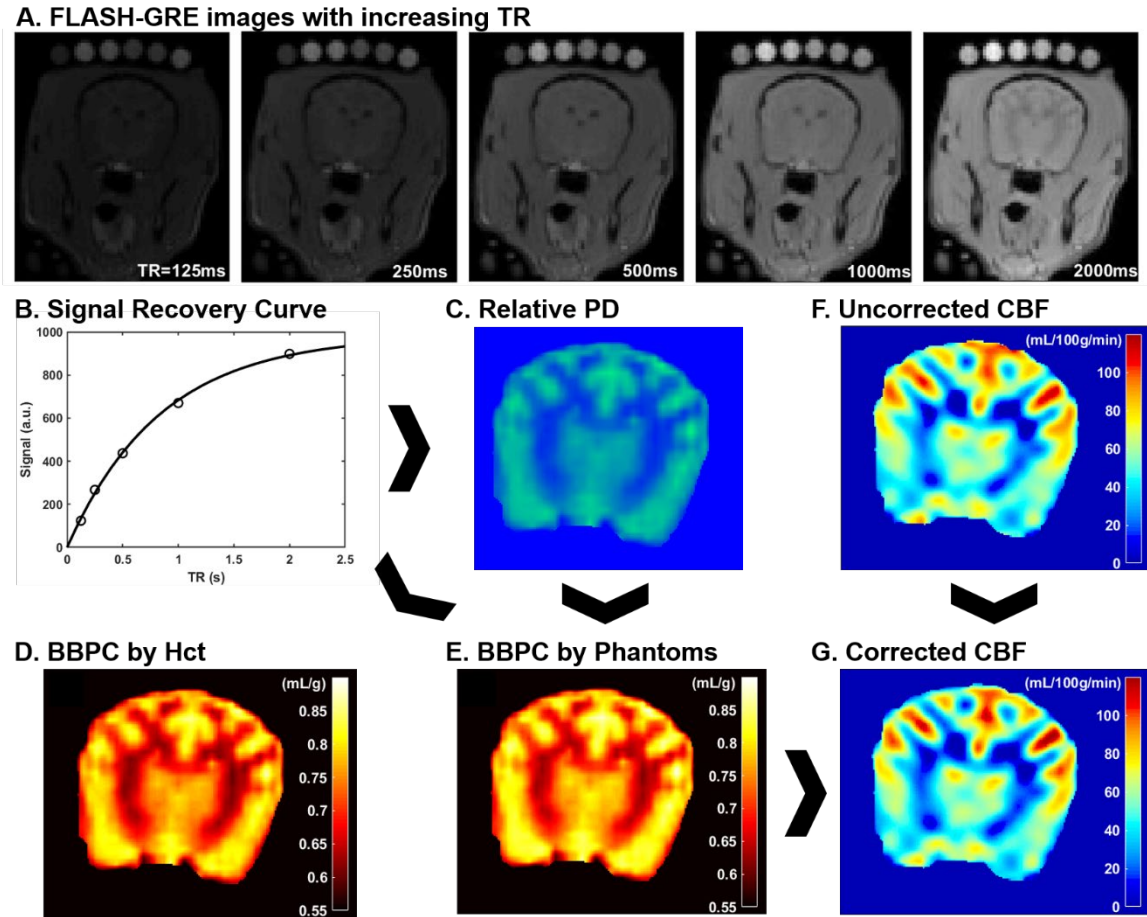


Figure 4.1 Explanation of CaSTRR and pCASL methods used in this study. CaSTRR utilizes a series of FLASH-GRE acquisitions with varying TR which include a blood sample and gadolinium-doped deuterium samples placed on the head (A). An exponential regression is fit to the signal recovery curve for each voxel (B) yielding a map of relative proton density values (C). The relative proton density values are calibrated using either water content estimated from hematocrit (D) or the scale of water content present in the phantoms (E). Uncorrected CBF maps are derived from pCASL acquisitions (F) and are corrected on a voxel-wise basis using the BBPC map normalized to the phantoms to create a corrected map of CBF (G).

Qualitative proton density maps were calculated in a voxel-wise manner by fitting the signal recovery curve to the mono-exponential equation $S = M_0 * [1 - e^{-(TR/T_1)}]$ to yield a map of M_0 in arbitrary units. Next a Bayesian bias field correction was applied to the M_0 maps to account for inhomogeneity in the receiver coil profile [135]. The low spatial

frequency bias field was calculated using 4th order polynomials and 6 Gaussian components, and to avoid artificially attenuating the higher signal water phantoms, the phantoms were excluded from the bias field estimation. (Fig. 4.1-B,C)

The M_0 maps were calibrated to absolute water content in two ways. The first follows the previously published CaSTRR technique which uses a series of 5 phantoms containing mixtures of deuterium oxide and distilled water at 40, 30, 20, 10, and 0% [134]. Because the deuterium oxide does not produce signal in MRI this creates a scale of known water concentration from 60-100% water. These phantoms were also doped with 0.18mM gadobutrol (Gadavist, Bayer Healthcare Pharmaceuticals, Whippany NJ, USA) to reduce the longitudinal relaxation rate (T1) to be similar to the T1 of brain tissue ($\approx 1.2s$). Next a linear regression was calculated based on the average M_0 value in each phantom and its known water content, and every voxel in the image was normalized to the resultant equation. However, we observed a quadratic relationship between the average M_0 values of the tissues and the average M_0 value of the phantoms such that the relationship between phantom proton density and tissue proton density was not constant. In order to correct for this, the quadratic term of the relationship was subtracted from the blood and tissue M_0 values prior to normalization. (Fig. 4.1-E)

The second method of calibrating M_0 maps utilized the hematocrit value to determine the absolute water content of the blood sample. Water content was determined according to the equation $WC_{blood} = -0.271 * Hct + 0.912$ [136]. The M_0 image was then normalized such that the average water content in the blood sample matched the average value calculated according to hematocrit.

BBPC maps were generated for both normalization methods by comparing the measured water content of each voxel in the brain to the average water content of the blood using the equation $BBPC = WC_{brain}/(WC_{blood}*1.04g/mL)$. (**Fig. 4.1-D**)

4.2.4 Cerebral Blood Flow and Anatomical Imaging

The CBF maps were acquired using a pCASL sequence with a three-dimensional gradient and spin echo (GRASE) readout [53]. The acquisition parameters were as follows: TR/TE/TI = 3200/16/1400 ms, field of view = 270 x 250 x 90 mm, matrix = 96 x 88, resolution = 3 x 3 x 3 mm, acquisition time = 6:15 minutes. (**Fig. 4.1-F**)

Because the original CBF maps were created with an assumed BBPC value of 0.9 mL/g, corrected maps were generated by dividing the entire map by this value and then multiplying by the BBPC map in a voxel-wise manner. BBPC correction was performed using the BBPC maps generated using the gadolinium doped water phantoms. (**Fig. 4.1-G**)

Contrast to noise ratio (CNR) was calculated according to the equation $CNR = (Mean_{gray} - Mean_{white})/Pooled\ Standard\ Deviation$ [137].

Anatomical images were acquired using a high resolution T1 weighted magnetization prepared rapid acquisition gradient echo (MPRAGE) sequence as recommended for optimal use with FreeSurfer [138]. Scan parameters were: TR/TE= 1690/2.56 ms, flip angle = 12°, field of view = 320 x 320 x 160 mm, matrix = 256 x 256 x 128, resolution = 0.8 x 0.8 x 0.8 mm, acquisition time = 10:49 minutes.

4.2.5 Image Analysis

All images were coregistered by first resampling the anatomical volumes to match the slice thickness of the CaSTRR and pCASL acquisitions. The CaSTRR and pCASL volumes were then registered to the anatomical using an intensity-based registration algorithm in Matlab (Mathworks, Natick MA, USA) [139]. The brain region of interest was extracted manually, and then segmented into gray and white regions of interest using an expectation maximization algorithm with classes for gray matter, white matter, and cerebrospinal fluid [140]. To avoid partial volume effects, the gray and white matter regions of interest in each slice were eroded by two pixels. Due to image inhomogeneities in the MPRAGE acquisitions in some animals, the segmentation algorithm often failed to adequately segment gray and white matter regions in the most rostral and caudal sections of the brain. While the BBPC maps did not display these inhomogeneities, the regions of interest were not reliable for analysis. For this reason, we chose to include only the centermost 10 slices in our analysis. These regions of interest were then applied to the BBPC and CBF maps. All image analysis was performed in Matlab (Mathworks, Natick MA, USA).

4.2.6 Statistical Analysis

All statistical analysis was performed in Matlab. Data is expressed as mean \pm standard deviation. Gray and white matter comparisons were assessed using three-way analysis of covariance with age, sex, and tissue type as independent variables. Linear regressions against age were also controlled for sex. Values of $p < 0.05$ were considered statistically significant.

4.3 Results

4.3.1 BBPC is Higher in Gray Matter than in White Matter

The first comparison was drawn on BBPC maps generated using the previously published CaSTRR method of normalizing to the gadolinium doped water phantoms (**Fig. 4.1-E**). The average BBPC in gray matter was 0.83 ± 0.05 mL/g which is 5.6% higher than the BBPC in white matter (0.78 ± 0.04 mL/g, $p = 0.007$) (**Fig. 4.2-B**). When plotted against age, neither the gray nor the white matter regions of interest demonstrated a significant correlation over the age range studied (gray matter: $p = 0.645$, white matter: $p = 0.483$).

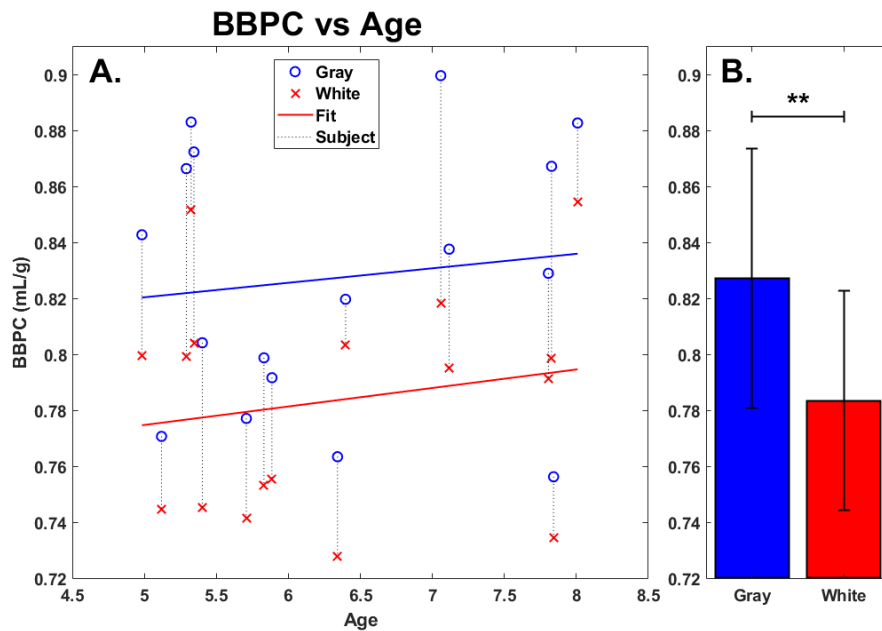


Figure 4.2 Average BBPC vs Age. Gray matter (blue) and white matter (red) regions of interest are plotted against age (A) and as group averages (B). Regions corresponding to the same animal are connected with a vertical dotted line. No significant linear correlation to age was found in either region. Average BBPC in gray matter was 5.6% higher than in white matter ($BBPC_{\text{gray}} = 0.83 \pm 0.05$ mL/g, $BBPC_{\text{white}} = 0.78 \pm 0.04$ mL/g, ** indicates $p < 0.01$, error bars represent 1 standard deviation)

4.3.2 Gray Matter CBF is Negatively Correlated with Age

Next, gray and white matter perfusion were compared in uncorrected CBF maps (**Fig. 4.1-F**) and again in corrected CBF maps (**Fig. 4.1-G**) which used the standard CaSTRR derived BBPC maps for correction (**Fig. 4.1-E**). Gray matter has 45% higher CBF than white matter in the uncorrected CBF maps ($CBF_{\text{gray}} = 81 \pm 12 \text{ mL}/100\text{g}/\text{min}$, $CBF_{\text{white}} = 56 \pm 12 \text{ mL}/100\text{g}/\text{min}$, $p < 0.001$) and 53% higher CBF in the maps corrected for BBPC ($cCBF_{\text{gray}} = 73 \pm 13 \text{ mL}/100\text{g}/\text{min}$, $cCBF_{\text{white}} = 49 \pm 11 \text{ mL}/100\text{g}/\text{min}$, $p < 0.01$) (see Figure 3-B). Gray matter demonstrated a significant negative correlation with age with a reduction of $7.5 \pm 2.1 \text{ mL}/100\text{g}/\text{min}$ each year or 9% of the average perfusion ($CBF_{\text{gray}} = 128 - 7.5 * \text{Age mL}/100\text{g}/\text{min}$, $p = 0.003$). The corrected CBF maps also revealed a reduction of $6.6 \pm 2.6 \text{ mL}/100\text{g}/\text{min}/\text{yr}$ ($cCBF_{\text{gray}} = 117 - 6.6 * \text{Age mL}/100\text{g}/\text{min}$, $p = 0.02$), but this relationship was not significantly different in the corrected maps than the uncorrected ($p = 0.81$). While there appears to be a downward trend in white matter perfusion with age, this correlation was not statistically significant in the uncorrected CBF maps ($p = 0.20$) or the corrected maps ($p = 0.33$) (**Fig. 4.3-A**).

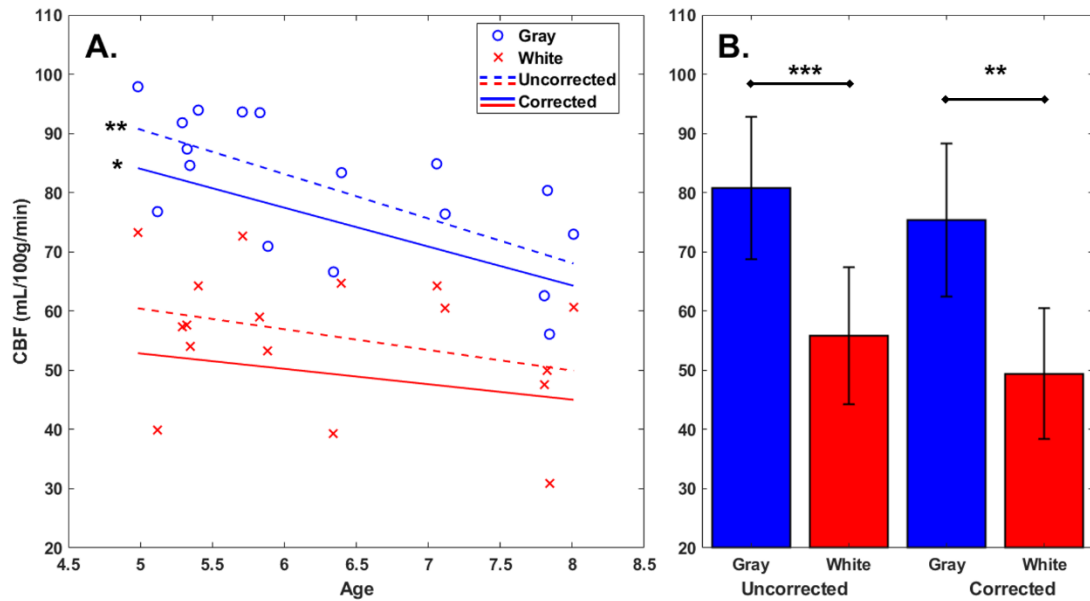


Figure 4.3 Gray and White CBF versus Age (A). Plotted points represent uncorrected average CBF for each animal. Gray matter CBF demonstrates a negative linear correlation with age in both uncorrected CBF maps ($CBF_{gray} = 128 - 7.5 * Age$ mL/100g/min) and maps corrected using measured BBPC ($cCBF_{gray} = 117 - 6.6 * Age$ mL/100g/min). Linear regression was not significant in the white matter region in either case. When considered as group averages (B), the gray matter has significantly higher CBF in both uncorrected ($CBF_{gray} = 81 \pm 12$ mL/100g/min, $CBF_{white} = 56 \pm 12$ mL/100g/min), and corrected maps ($cCBF_{gray} = 73 \pm 13$ mL/100g/min, $cCBF_{white} = 49 \pm 11$ mL/100g/min). (* indicates $p < 0.05$, ** indicates $p < 0.01$, *** indicates $p < 0.001$, error bars represent 1 standard deviation.

4.3.3 BBPC Correction improves contrast to noise ratio in CBF maps

Next, the CNR of corrected CBF maps (**Fig. 4.1-G**) was compared to uncorrected CBF maps (**Fig. 4.1-F**). On average BBPC correction improved CNR between gray and white matter regions of the CBF maps by 3.6% (95% confidence interval = 0.6 – 6.5%). The average uncorrected CNR was 0.81 and the average corrected CNR was 0.84.

4.3.4 BBPC Values Generated Using Hematocrit Agree with Values Generated Using Phantoms

The final comparison was between maps normalized using the doped water phantoms (**Fig. 4.1-E**) to ones normalized using hematocrit derived blood water content (**Fig. 4.1-D**), we observed positive correlations between the BBPC values generated using these two methods. The Pearson correlation was $R^2 = 0.81$ for gray matter indicating strong correlation between these measures in this region (**Fig. 4.4-A**). Due to higher variability in the white matter regions the correlation was moderate in white matter ($R^2 = 0.59$) (see **Fig. 4.4-C**). The measured BBPC values were slightly lower in maps normalized to hematocrit, though not statistically different, and Bland-Altman analysis demonstrates no significant bias in either region of interest (**Fig. 4.4-B,D**). Again the BBPC in gray matter was 5.9% higher than in white matter when using hematocrit to normalize ($BBPC_{\text{gray}} = 0.81 \pm 0.06$ mL/g, $BBPC_{\text{white}} = 0.77 \pm 0.05$ mL/g, $p = 0.02$).

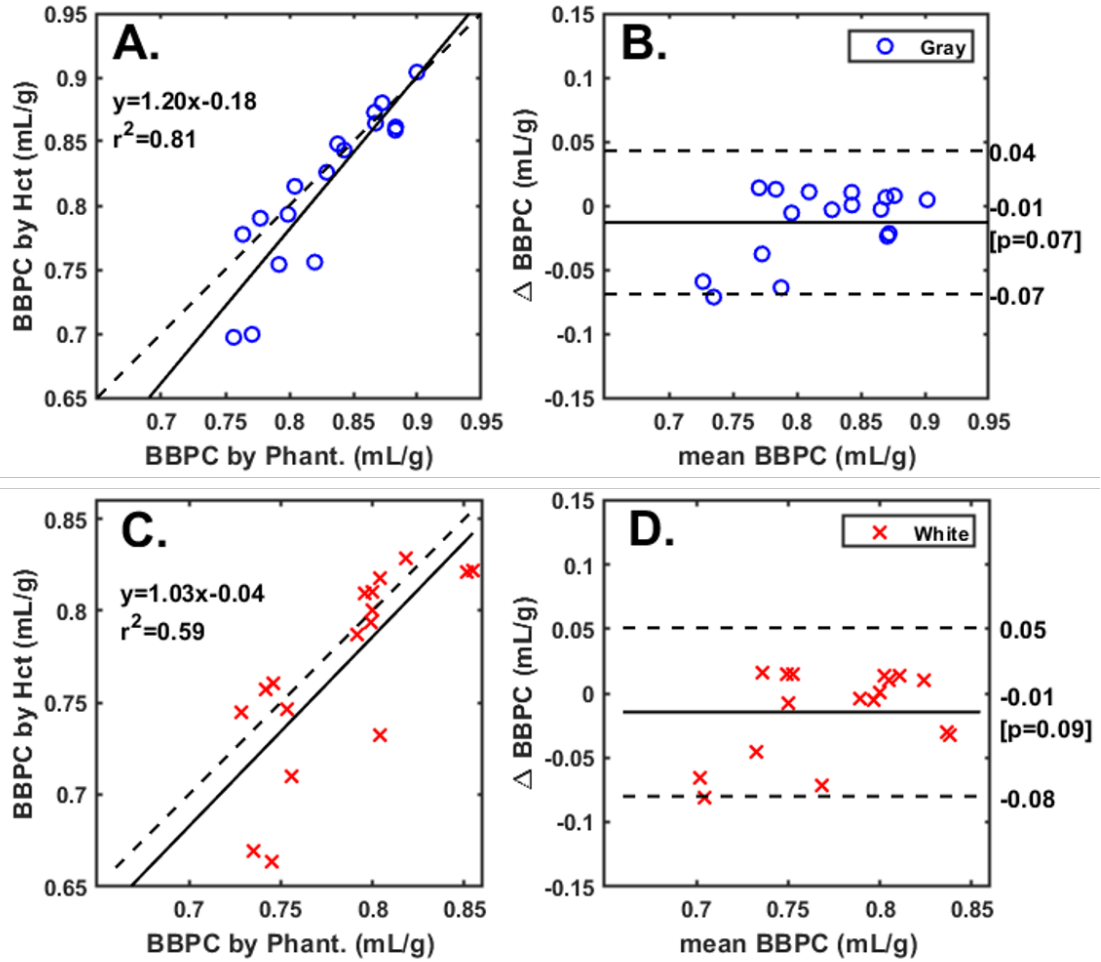


Figure 4.4 Correlation of BBPC values in maps normalized according to hematocrit with values in maps normalized to the gadolinium-doped phantoms. Correlation is very strong for the gray matter BBPC values ($R^2 = 0.81$) (A) and moderately strong for white matter ($R^2 = 0.59$) (C). Bland-Altman analysis demonstrates no significant bias in either gray (B) or white matter values (D).

4.4 Discussion

The CaSTRR technique represents a significant improvement in the acquisition speed of BBPC maps. A previously published report measuring BBPC using a 1.5T human scanner acquired a single slice of the BBPC map in approximately 30 minutes [58]. In this study we were able to produce BBPC maps of sufficient quality to perform voxel-wise correction of CBF maps with coverage of the entire brain using a CaSTRR acquisition

protocol that only required 4 minutes of scan time. This is an improvement over the reported CaSTRR technique in mice which required 17 minutes of scan time due to the much higher resolution requirement of scanning small animals at 7T [134]. A four minute scan time is comparable to the acquisition time of the pCASL technique for CBF. The experiment was also done with commercially available equipment and pulse sequences that are directly applicable for use with a human subject. Furthermore, the CaSTRR scans were performed with the same birdcage receive coil that was used for the pCASL acquisitions. This was not possible when scanning mice at 7T and represents a significant advantage of scanning at lower fields. The greatly reduced scan time and ready availability of equipment and pulse sequences demonstrate that CaSTRR is a feasible approach to correct CBF maps using empirically measured BBPC values instead of assuming a constant value for all tissue types, pathologies, ages, and species. This technique has the potential for rapid translation to use in human studies.

While BBPC has not been previously reported in canines, our reported values of 0.83 ± 0.05 mL/g in gray matter and 0.78 ± 0.04 mL/g in white matter are lower than published reports in humans, non-human primates, and mice [57, 61, 62]. One possible reason for this is the temperature discrepancy between the blood sample and the brain tissue. When measured at room temperature instead of physiologic temperature, the proton density of the blood could be overestimated by as much as 5% causing BBPC to be underestimated by the same amount [141]. The amount of inter-species variability in BBPC values is further evidence for the importance of empirical BBPC correction when quantifying CBF.

The correlation between the two methods of normalization represents a distinct advantage of this study. Our results suggest that the CaSTRR technique can be further simplified by omitting the gadolinium doped water phantoms. This would also obviate the need for correcting the non-linear signal increases observed in the water phantoms in this study.

Another significant advantage of this study is the use of Bayesian bias field correction to account for inhomogeneities in the receiver coil sensitivity profile. The CaSTRR method described in mice assumed a sufficiently homogenous profile in the birdcage receive coil, but observed significant signal loss near the large ear canals of the mouse [134]. Other BBPC studies attempted to correct for bias field using a separate measurement on a uniform phantom [58, 62], but it is unlikely that the receiver profile would be the same when measuring the non-uniform tissue of a live subject.

Arterial spin labeling has an inherently low signal to noise ratio because it is a subtractive technique. Including an empirical measurement of BBPC to the quantification of CBF will increase noise, as we observed in the greater variance of CBF values in the corrected maps. However, there was an improvement in contrast to noise between areas with significantly different BBPC values despite this addition of noise. This could become important when studying perfusion in models of pathology where the tissue composition is likely to change.

There are many examples of pathologies that could affect water balance in the brain. Brain edema caused by ischemia [142], infection [143], or trauma [144] can cause localized increases in free water and potentially affect the BBPC. Another important field of interest where ASL is commonly used is the study of Alzheimer's disease (AD). The

deposition of hydrophobic amyloid- β protein, which is a hallmark of AD pathology, may reduce the BBPC in regions of plaque development [145]. AD occurs in the context of aging and typically causes pronounced brain atrophy [146]. Both of these could result in reduced brain water content and therefore reduced BBPC. Both brain volume [147] and hematocrit [148] can also change significantly with a subject's level of hydration. So while our result showed that BBPC correction did not affect the observed relationship between CBF and age between the ages of 5-8 year, it is possible that BBPC correction could improve sensitivity in studies where BBPC is expected to change significantly. In future studies, CaSTRR imaging could be used to study how BBPC changes with pathology and could also be used to account for water balance effects when measuring perfusion.

In conclusion, this study demonstrates the feasibility of CaSTRR as a method to correct CBF measurements for regional and inter-subject variability in BBPC, and demonstrates the potential for use in human studies.

CHAPTER 5. DISCUSSION

5.1 Overview

The impetus of this dissertation project was a clinical hypothesis regarding cerebral perfusion in the setting of Down syndrome (DS). Namely, we hypothesized that people with DS would have compromised cerebral blood flow (CBF) despite a protective cardiovascular risk profile. In the study described in chapter 2, we were able to demonstrate reduced CBF in people with DS over the age of 54 years. This represents the first quantitative perfusion imaging study in DS and is particularly interesting for the delayed pattern of perfusion deficits in this population. This had not been described previously and contrasts with the typical pattern of early CBF deficits in familial Alzheimer's disease (AD).

However, limitations in the currently available methods to measure brain-blood partition coefficient (BBPC) prevented us from accounting for potential changes in brain water content. Such changes could arise in the setting of DS or AD from aging, atrophy, or the deposition of hydrophobic amyloid- β (A- β) plaques. This prompted the development of the rapid BBPC method described in chapter 3. Calibrated short TR recovery (CaSTRR) imaging in mice reduced acquisition time by 87% and improved contrast between gray and white matter regions in corrected CBF maps.

The CaSTRR technique was then translated for use with equipment suitable for humans in chapter 4. Healthy canines were scanned using the same protocol and equipment as would be used with human subjects. This study represents the first report of BBPC values in canines and establishes a negative correlation between gray matter perfusion and age. Further improvements are also made to the CaSTRR protocol such that acquisition

time is reduced to 4 minutes and it is demonstrated that gadolinium-doped phantoms are not necessary because hematocrit can serve as a proxy value for blood water content. These simplifications and the results of this study demonstrate the feasibility of using CaSTRR for empirical BBPC correction of CBF maps.

5.2 Future Directions

Despite the improvements, there are still limitations that will need to be addressed in the future. First the CaSTRR technique requires a sample of the subject's blood to be placed in the scanner during acquisition. While drawing a blood sample is a routine procedure, future advancements to obviate this step would further simplify the method. This could potentially be accomplished by acquiring higher resolution CaSTRR images such that the water content of the blood could be measured in the sagittal sinus of the image. In our studies of mice and dogs, the sagittal sinuses were not large enough to accomplish this, but it may be possible to do so with the larger anatomy of a human. Pulsatile flow in the sagittal sinuses poses a challenge to such a strategy, however the constant inflow of unsaturated blood may result in a flat signal recovery curve from which the blood water content may be determined. Second, the post-processing of CaSTRR images to create BBPC maps and use them to correct CBF maps is not currently optimized. The final corrected CBF map is a result of several steps of coregistration and performing an exponential regression on every voxel in the CaSTRR acquisition. This is computationally expensive and would benefit from optimization in the future. Image analysis is also currently limited to semi-automated methods that require user input. Fully-automated methods would drastically reduce post-processing time.

Having established proof of concept in both small animal scanners and human scanners, the next step will be to apply the CaSTRR technique in clinical and pre-clinical settings where BBPC is expected to change. While the final translational step to application in humans remains for future studies, the results of chapter 4 are promising that CaSTRR will be effective in humans as it has been in mice and dogs. Once accomplished there are a variety of pathologies and small animal models of disease to which CaSTRR imaging could be applied.

For example, there are numerous studies in humans and small animals that use ASL to track perfusion in AD. It is reasonable to think that atrophy and A- β accumulation could affect brain water content in this disease, so CaSTRR represents a potential tool to track changes in BBPC over time and determine the sensitivity of ASL to those changes. Because ASL and CaSTRR imaging are non-invasive and non-radiative, they are well suited for use in longitudinal studies.

The original clinical question of this dissertation concerned DS and we recognized the inability to account for BBPC variability as a limitation of that study. It would be appropriate to apply CaSTRR as a method to overcome that limitation and determine if there is a change in BBPC concomitant with the observed change in CBF. While small animal models of DS do exist, they are often challenging to correlate with the human condition. However, due to the simplicity of CaSTRR it is feasible to include this method as part of ongoing clinical experiments that already use MRI.

Other pathologies or treatments could yield significant changes in BBPC as well. Brain edema as the result of ischemic injury, cranial trauma, or infection could have acute, local effects on BBPC. These would be an interesting application of CaSTRR to determine if excess free water could confound CBF deficits measured by ASL. There is also some preliminary evidence that pharmacological treatment could affect BBPC. When treated with rapamycin, mice demonstrate an increase in BBPC in the hippocampus. This could be significant when considering the role of ASL to track treatment efficacy, and it highlights the importance of controlling for BBPC variability using a technique like CaSTRR.

5.3 Innovation

The results presented in this dissertation represent a significant advancement to the fields of neuroimaging and neuroscience in the following ways. First, the study in chapter 2 is the first to demonstrate compromised perfusion in people with DS despite their lack of typical risk factors for cerebrovascular disease. This contributes to the understanding of the role of cerebrovascular disease in the progression of AD. Second, the development of the CaSTRR technique overcomes the significant limitation of excessively long scan times to measure BBPC. This allows for more accurate quantification of CBF using BBPC correction, which is particularly important when studying pathologies where brain water content is likely to be disrupted. The results from chapters 3 and 4 demonstrate the benefit of CaSTRR to improve contrast in CBF maps. Third, the results of chapter 4 represent the first report of BBPC values in canines. These vary from the values reported for humans, mice, and monkeys highlighting the importance of using empirical values for BBPC when quantifying CBF. Finally, the CaSTRR technique was translated in chapter 4 for future use with human subjects. This demonstrate the great translational value of this project, which

spans three species and has produced a valuable technique for use in both clinical and pre-clinical research.

5.4 Conclusion

In summary, we have shown that MRI-based CBF measurement is a valuable method to identify neuronal disease progression in pathologies like DS. However, a traditional assumption of constant BBPC has limited CBF studies from accounting for the potential confounding factor of changes in brain water content. We addressed this issue with the development of novel CaSTRR methods, which can be applied in both animal and human scanners. With this improvement, it is expected that CBF can be even more sensitive to neuronal function changes and in the future will serve as invaluable biomarker for identifying disease progression and treatment efficacy.

REFERENCES

1. Moniz, E., *Arterial encephalography: importance in the localization of cerebral tumors*. Rev Neurol (Paris), 1927. **2**(1): p. 72-90.
2. Gbd, M. and C. Causes Of Death, *Global, regional, and national life expectancy, all-cause mortality, and cause-specific mortality for 249 causes of death, 1980–2015: a systematic analysis for the Global Burden of Disease Study 2015*. 2016: p. 1459-1544. ISSN 0140-6736.
3. Heron, M., *Deaths: Leading Causes for 2014*. Natl Vital Stat Rep, 2016. **65**(5): p. 1-96.
4. Powers, W.J., *Imaging preventable infarction in patients with acute ischemic stroke*. AJNR Am J Neuroradiol, 2008. **29**(10): p. 1823-5.
5. Chalela, J.A., et al., *Magnetic resonance perfusion imaging in acute ischemic stroke using continuous arterial spin labeling*. Stroke, 2000. **31**(3): p. 680-7.
6. Guo, L., et al., *Pseudo-continuous arterial spin labeling quantifies cerebral blood flow in patients with acute ischemic stroke and chronic lacunar stroke*. Clin Neurol Neurosurg, 2014. **125**: p. 229-36.
7. Wolf, R.L., et al., *Arteriovenous shunt visualization in arteriovenous malformations with arterial spin-labeling MR imaging*. AJNR Am J Neuroradiol, 2008. **29**(4): p. 681-7.
8. Le, T.T., et al., *Identification of venous signal on arterial spin labeling improves diagnosis of dural arteriovenous fistulas and small arteriovenous malformations*. AJNR Am J Neuroradiol, 2012. **33**(1): p. 61-8.
9. Albers, G.W., et al., *Magnetic resonance imaging profiles predict clinical response to early reperfusion: the diffusion and perfusion imaging evaluation for understanding stroke evolution (DEFUSE) study*. Ann Neurol, 2006. **60**(5): p. 508-17.
10. Pollock, J.M., et al., *Response of arteriovenous malformations to gamma knife therapy evaluated with pulsed arterial spin-labeling MRI perfusion*. AJR Am J Roentgenol, 2011. **196**(1): p. 15-22.
11. Hays, C.C., Z.Z. Zlatar, and C.E. Wierenga, *The Utility of Cerebral Blood Flow as a Biomarker of Preclinical Alzheimer's Disease*. Cell Mol Neurobiol, 2016. **36**(2): p. 167-79.
12. Du, A.T., et al., *Hypoperfusion in frontotemporal dementia and Alzheimer disease by arterial spin labeling MRI*. Neurology, 2006. **67**(7): p. 1215-20.
13. Schuff, N., et al., *Cerebral blood flow in ischemic vascular dementia and Alzheimer's disease, measured by arterial spin-labeling magnetic resonance imaging*. Alzheimers Dement, 2009. **5**(6): p. 454-62.
14. Fleisher, A.S., et al., *Cerebral perfusion and oxygenation differences in Alzheimer's disease risk*. Neurobiol Aging, 2009. **30**(11): p. 1737-48.
15. Okonkwo, O.C., et al., *Cerebral blood flow is diminished in asymptomatic middle-aged adults with maternal history of Alzheimer's disease*. Cereb Cortex, 2014. **24**(4): p. 978-88.
16. Xiu, J., et al., *Prognostic Value of Myocardial Perfusion Analysis in Patients with Coronary Artery Disease: A Meta-Analysis*. J Am Soc Echocardiogr, 2017. **30**(3): p. 270-281.

17. Roberts, D.A., et al., *Renal perfusion in humans: MR imaging with spin tagging of arterial water*. Radiology, 1995. **196**(1): p. 281-6.
18. Kety, S.S. and C.F. Schmidt, *THE NITROUS OXIDE METHOD FOR THE QUANTITATIVE DETERMINATION OF CEREBRAL BLOOD FLOW IN MAN: THEORY, PROCEDURE AND NORMAL VALUES*. The Journal of clinical investigation, 1948. **27**(4): p. 476.
19. Lassen, N.A. and D.H. Ingvar, *The blood flow of the cerebral cortex determined by radioactive krypton*. Experientia, 1961. **17**: p. 42-3.
20. Yonas, H., et al., *Stable xenon CT/CBF imaging: laboratory and clinical experience*. Adv Tech Stand Neurosurg, 1987. **15**: p. 3-37.
21. Neirinckx, R.D., *Evaluation of regional cerebral blood flow with ^{99m}Tc-d, 1 HM-PAO and SPECT*. Neurosurg Rev, 1987. **10**(3): p. 181-4.
22. Herscovitch, P., J. Markham, and M.E. Raichle, *Brain blood flow measured with intravenous H₂(15)O. I. Theory and error analysis*. J Nucl Med, 1983. **24**(9): p. 782-9.
23. Axel, L., *Cerebral blood flow determination by rapid-sequence computed tomography: theoretical analysis*. Radiology, 1980. **137**(3): p. 679-86.
24. Villringer, A., et al., *Dynamic imaging with lanthanide chelates in normal brain: contrast due to magnetic susceptibility effects*. Magn Reson Med, 1988. **6**(2): p. 164-74.
25. Williams, D.S., et al., *Magnetic Resonance Imaging of Perfusion Using Spin Inversion of Arterial Water*. Proceedings of the National Academy of Sciences of the United States of America, 1992. **89**(1): p. 212-216.
26. Wong, E.C., R.B. Buxton, and L.R. Frank, *Implementation of quantitative perfusion imaging techniques for functional brain mapping using pulsed arterial spin labeling*. NMR Biomed, 1997. **10**(4-5): p. 237-49.
27. Wong, E.C., R.B. Buxton, and L.R. Frank, *Quantitative imaging of perfusion using a single subtraction (QUIPSS and QUIPSS II)*. Magn Reson Med, 1998. **39**(5): p. 702-8.
28. Dai, W., et al., *Continuous flow-driven inversion for arterial spin labeling using pulsed radio frequency and gradient fields*. Magn Reson Med, 2008. **60**(6): p. 1488-97.
29. Buxton, R.B., et al., *A general kinetic model for quantitative perfusion imaging with arterial spin labeling*. Magn Reson Med, 1998. **40**(3): p. 383-96.
30. Leoni, R.F., et al., *Cerebral blood flow and vasoreactivity in aging: an arterial spin labeling study*. Braz J Med Biol Res, 2017. **50**(4): p. e5670.
31. Parkes, L.M., et al., *Normal cerebral perfusion measurements using arterial spin labeling: reproducibility, stability, and age and gender effects*. Magn Reson Med, 2004. **51**(4): p. 736-43.
32. Siewert, B., et al., *Comparison of EPISTAR and T2*-weighted gadolinium-enhanced perfusion imaging in patients with acute cerebral ischemia*. Neurology, 1997. **48**(3): p. 673-9.
33. Detre, J.A., et al., *Noninvasive MRI evaluation of cerebral blood flow in cerebrovascular disease*. Neurology, 1998. **50**(3): p. 633-41.
34. Wu, R.H., et al., *MR measurement of regional relative cerebral blood volume in epilepsy*. J Magn Reson Imaging, 1999. **9**(3): p. 435-40.

35. Wolf, R.L., et al., *Detection of mesial temporal lobe hypoperfusion in patients with temporal lobe epilepsy by use of arterial spin labeled perfusion MR imaging*. AJNR Am J Neuroradiol, 2001. **22**(7): p. 1334-41.
36. Lin, C.M., et al., *Arterial Spin Labeling Perfusion Study in the Patients with Subacute Mild Traumatic Brain Injury*. PLoS One, 2016. **11**(2): p. e0149109.
37. Peng, S.P., et al., *Pulsed arterial spin labeling effectively and dynamically observes changes in cerebral blood flow after mild traumatic brain injury*. Neural Regen Res, 2016. **11**(2): p. 257-61.
38. Alsop, D.C., J.A. Detre, and M. Grossman, *Assessment of cerebral blood flow in Alzheimer's disease by spin-labeled magnetic resonance imaging*. Ann Neurol, 2000. **47**(1): p. 93-100.
39. Sandson, T.A., et al., *Noninvasive perfusion MRI in Alzheimer's disease: a preliminary report*. Neurology, 1996. **47**(5): p. 1339-42.
40. Gaa, J., et al., *Noninvasive perfusion imaging of human brain tumors with EPISTAR*. Eur Radiol, 1996. **6**(4): p. 518-22.
41. Warmuth, C., M. Gunther, and C. Zimmer, *Quantification of blood flow in brain tumors: comparison of arterial spin labeling and dynamic susceptibility-weighted contrast-enhanced MR imaging*. Radiology, 2003. **228**(2): p. 523-32.
42. Weber, M.A., et al., *Diagnostic performance of spectroscopic and perfusion MRI for distinction of brain tumors*. Neurology, 2006. **66**(12): p. 1899-906.
43. Wang, J. and D.J. Licht, *Pediatric perfusion MR imaging using arterial spin labeling*. Neuroimaging Clin N Am, 2006. **16**(1): p. 149-67, ix.
44. Oguz, K.K., et al., *Sickle cell disease: continuous arterial spin-labeling perfusion MR imaging in children*. Radiology, 2003. **227**(2): p. 567-74.
45. Licht, D.J., et al., *Preoperative cerebral blood flow is diminished in neonates with severe congenital heart defects*. J Thorac Cardiovasc Surg, 2004. **128**(6): p. 841-9.
46. Guo, Y., et al., *Age and brain region associated alterations of cerebral blood flow in early Alzheimer's disease assessed in AbetaPPSWE/PS1DeltaE9 transgenic mice using arterial spin labeling*. Mol Med Rep, 2019. **19**(4): p. 3045-3052.
47. Lin, A.L., et al., *Rapamycin rescues vascular, metabolic and learning deficits in apolipoprotein E4 transgenic mice with pre-symptomatic Alzheimer's disease*. J Cereb Blood Flow Metab, 2015.
48. Foley, L.M., et al., *MRI assessment of cerebral blood flow after experimental traumatic brain injury combined with hemorrhagic shock in mice*. J Cereb Blood Flow Metab, 2013. **33**(1): p. 129-36.
49. Hattori, Y., et al., *Gradual Carotid Artery Stenosis in Mice Closely Replicates Hypoperfusive Vascular Dementia in Humans*. J Am Heart Assoc, 2016. **5**(2).
50. Pham, M., et al., *Outcome of experimental stroke in C57Bl/6 and Sv/129 mice assessed by multimodal ultra-high field MRI*. Exp Transl Stroke Med, 2010. **2**: p. 6.
51. Schraml, C., et al., *Perfusion imaging of the pancreas using an arterial spin labeling technique*. J Magn Reson Imaging, 2008. **28**(6): p. 1459-65.
52. Pan, X., et al., *Quantification of liver perfusion using multidelay pseudocontinuous arterial spin labeling*. J Magn Reson Imaging, 2016. **43**(5): p. 1046-54.
53. Alsop, D.C., et al., *Recommended implementation of arterial spin-labeled perfusion MRI for clinical applications: A consensus of the ISMRM perfusion study*

- group and the European consortium for ASL in dementia. *Magn Reson Med*, 2015. **73**(1): p. 102-16.
54. Fick, A., *Über die Messung des Blutquantums in der Herzventrikeln*. Sitz der Physik-Med Ges Würzburg, 1870. **2**(1): p. 16-28.
 55. Wong, E.C., R.B. Buxton, and L.R. Frank, *A theoretical and experimental comparison of continuous and pulsed arterial spin labeling techniques for quantitative perfusion imaging*. *Magn Reson Med*, 1998. **40**(3): p. 348-55.
 56. Lu, H., et al., *Determining the longitudinal relaxation time (T1) of blood at 3.0 Tesla*. *Magn Reson Med*, 2004. **52**(3): p. 679-82.
 57. Herscovitch, P. and M.E. Raichle, *What is the correct value for the brain--blood partition coefficient for water?* *J Cereb Blood Flow Metab*, 1985. **5**(1): p. 65-9.
 58. Roberts, D.A., et al., *Magnetic resonance imaging of the brain: blood partition coefficient for water: application to spin-tagging measurement of perfusion*. *J Magn Reson Imaging*, 1996. **6**(2): p. 363-6.
 59. Iida, H., et al., *A determination of the regional brain/blood partition coefficient of water using dynamic positron emission tomography*. *J Cereb Blood Flow Metab*, 1989. **9**(6): p. 874-85.
 60. Hirata, K., et al., *Regional partition coefficient of water in patients with cerebrovascular disease and its effect on rCBF assessment*. *Nucl Med Commun*, 2011. **32**(1): p. 63-70.
 61. Kudomi, N., et al., *Rapid quantitative measurement of CMRO(2) and CBF by dual administration of (15)O-labeled oxygen and water during a single PET scan-a validation study and error analysis in anesthetized monkeys*. *J Cereb Blood Flow Metab*, 2005. **25**(9): p. 1209-24.
 62. Leithner, C., et al., *Determination of the brain-blood partition coefficient for water in mice using MRI*. *J Cereb Blood Flow Metab*, 2010. **30**(11): p. 1821-4.
 63. Ballard, C., et al., *Dementia in Down's syndrome*. *Lancet Neurol*, 2016. **15**(6): p. 622-36.
 64. Schupf, N., Sergievsky, G.H., *Genetic and host factors for dementia in Down's syndrome*. *British journal of psychiatry*, 2002. **180**: p. 405-410.
 65. Jellinger, K.A., *Pathology and pathogenesis of vascular cognitive impairment-a critical update*. *Front Aging Neurosci*, 2013. **5**: p. 17.
 66. Parker, S.E., et al., *Updated National Birth Prevalence estimates for selected birth defects in the United States, 2004-2006*. *Birth Defects Res A Clin Mol Teratol*, 2010. **88**(12): p. 1008-16.
 67. Presson, A.P., et al., *Current estimate of Down Syndrome population prevalence in the United States*. *J Pediatr*, 2013. **163**(4): p. 1163-8.
 68. Batshaw, M.L., *Mental retardation*. *Pediatr Clin North Am*, 1993. **40**(3): p. 507-21.
 69. Glasson, E.J., et al., *The changing survival profile of people with Down's syndrome: implications for genetic counselling*. *Clin Genet*, 2002. **62**(5): p. 390-3.
 70. Bittles, A.H., et al., *The four ages of Down syndrome*. *Eur J Public Health*, 2007. **17**(2): p. 221-5.
 71. Head, E., et al., *Aging in Down Syndrome and the Development of Alzheimer's Disease Neuropathology*. *Curr Alzheimer Res*, 2016. **13**(1): p. 18-29.

72. Prasher, V.P., et al., *Molecular mapping of Alzheimer-type dementia in Down's syndrome*. *Ann Neurol*, 1998. **43**(3): p. 380-3.
73. Doran, E., et al., *Down Syndrome, Partial Trisomy 21, and Absence of Alzheimer's Disease: The Role of APP*. *J Alzheimers Dis*, 2017. **56**(2): p. 459-470.
74. Snyder, H.M., et al., *Vascular contributions to cognitive impairment and dementia including Alzheimer's disease*. *Alzheimers Dement*, 2015. **11**(6): p. 710-7.
75. Kapasi, A. and J.A. Schneider, *Vascular contributions to cognitive impairment, clinical Alzheimer's disease, and dementia in older persons*. *Biochim Biophys Acta*, 2016. **1862**(5): p. 878-86.
76. Provenzano, F.A., et al., *White matter hyperintensities and cerebral amyloidosis: necessary and sufficient for clinical expression of Alzheimer disease?* *JAMA Neurol*, 2013. **70**(4): p. 455-61.
77. Murdoch, J.C., Rodger, J.C., Rao, S.S., Fletcher, C.D., Dunningham, M.G., *Down's syndrome: an atheroma-free model?* . *Br Med J*, 1977. **2**(6081): p. 226-228.
78. Brattstrom, L., Englund, E., Brun, A., *Does Down syndrome support homocysteine theory of arteriosclerosis*. *Lancet*, 1987. **14**(8529): p. 391-392.
79. Yla-Herttuala, S., Luoma, J., Nikkari, T., Kivimaki, T., *Down's syndrome and atherosclerosis*. *Atherosclerosis*, 1989. **76**(2-3): p. 269-272.
80. Wilcock, D.M., F.A. Schmitt, and E. Head, *Cerebrovascular contributions to aging and Alzheimer's disease in Down syndrome*. *Biochim Biophys Acta*, 2016. **1862**(5): p. 909-14.
81. Attems, J., et al., *Review: sporadic cerebral amyloid angiopathy*. *Neuropathol Appl Neurobiol*, 2011. **37**(1): p. 75-93.
82. Ikeda, S., et al., *Variability of beta-amyloid protein deposited lesions in Down's syndrome brains*. *Tohoku J Exp Med*, 1994. **174**(3): p. 189-98.
83. Lai, F., and Williams, M.D., *A prospective study of Alzheimer Disease in Down Syndrome*. *Archives of Neurology*, 1989. **46**: p. 849-853.
84. Belza, M.G. and H. Urich, *Cerebral amyloid angiopathy in Down's syndrome*. *Clin Neuropathol*, 1986. **5**(6): p. 257-60.
85. Head, E., et al., *Cerebrovascular pathology in Down syndrome and Alzheimer disease*. *Acta Neuropathol Commun*, 2017. **5**(1): p. 93.
86. Helman, A.M., et al., *Microbleeds and Cerebral Amyloid Angiopathy in the Brains of People with Down Syndrome with Alzheimer's Disease*. *J Alzheimers Dis*, 2019. **67**(1): p. 103-112.
87. Petcharunpaisan, S., J. Ramalho, and M. Castillo, *Arterial spin labeling in neuroimaging*. *World J Radiol*, 2010. **2**(10): p. 384-98.
88. Powell, D., et al., *Frontal white matter integrity in adults with Down syndrome with and without dementia*. *Neurobiol Aging*, 2014.
89. Sparrow, S.S., D.V. Cicchetti, and D.A. Balla, *Vineland adaptive behavior scales: Second Edition (Vineland II), survey interview form/caregiver rating form*. 2005, Pearson Assessments: Livonia, MN.
90. Evenhuis, H.M., *Further evaluation of the Dementia Questionnaire for Persons with Mental Retardation (DMR)*. *J Intellect Disabil Res*, 1996. **40** (Pt 4): p. 369-73.
91. Cummings, J.L., et al., *The Neuropsychiatric Inventory: comprehensive assessment of psychopathology in dementia*. *Neurology*, 1994. **44**(12): p. 2308-14.

92. Panisset, M., et al., *Severe impairment battery. A neuropsychological test for severely demented patients*. Arch Neurol, 1994. **51**(1): p. 41-5.
93. Dalton, A.J., *The Dyspraxia Scale for adults with Down syndrome*, in *Neuropsychological Assessments of Dementia in Down Syndrome and Intellectual Disabilities*, V.P. Prasher, Editor. 2009, Springer London: London. p. 67-89.
94. Lowenstein, D., *The Fuld OME as a more culture-fair memory test in the elderly*. Clinical Gerontologist, 1995. **15**(4): p. 52-58.
95. McKhann, G., et al., *Clinical diagnosis of Alzheimer's disease: report of the NINCDS-ADRDA Work Group under the auspices of Department of Health and Human Services Task Force on Alzheimer's Disease*. Neurology, 1984. **34**(7): p. 939-944.
96. Dubois, B., et al., *Advancing research diagnostic criteria for Alzheimer's disease: the IWG-2 criteria*. Lancet Neurology, 2014. **13**(6): p. 614-629.
97. Jenks, G.F., *The Data Model Concept in Statistical Mapping*. International Yearbook of Cartography, 1967. **7**: p. 186-190.
98. Vinters, H.V., *Cerebral amyloid angiopathy. A critical review*. Stroke, 1987. **18**(2): p. 311-24.
99. Cenini, G., et al., *Association between frontal cortex oxidative damage and beta-amyloid as a function of age in Down syndrome*. Biochim Biophys Acta, 2012. **1822**(2): p. 130-8.
100. Zaharchuk, G., et al., *Arterial spin-label imaging in patients with normal bolus perfusion-weighted MR imaging findings: pilot identification of the borderzone sign*. Radiology, 2009. **252**(3): p. 797-807.
101. Wee, S., et al., *Carotid Vascular Blood Flow in Individuals with Down Syndrome Following Low Body Negative Pressure Challenge*. Faseb J., 2017. **31**(s1).
102. Hu, M., et al., *Arterial stiffness response to exercise in persons with and without Down syndrome*. Res Dev Disabil, 2013. **34**(10): p. 3139-47.
103. Rodrigues, A.N., et al., *Stiffness of the large arteries in individuals with and without Down syndrome*. Vasc Health Risk Manag, 2011. **7**: p. 375-81.
104. Holland, C.M., et al., *Spatial distribution of white-matter hyperintensities in Alzheimer disease, cerebral amyloid angiopathy, and healthy aging*. Stroke, 2008. **39**(4): p. 1127-33.
105. Brickman, A.M., *Contemplating Alzheimer's disease and the contribution of white matter hyperintensities*. Curr Neurol Neurosci Rep, 2013. **13**(12): p. 415.
106. Back, S.A., et al., *White matter lesions defined by diffusion tensor imaging in older adults*. Ann Neurol, 2011. **70**(3): p. 465-76.
107. Chao, L.L., et al., *Associations between white matter hyperintensities and beta amyloid on integrity of projection, association, and limbic fiber tracts measured with diffusion tensor MRI*. PLoS One, 2013. **8**(6): p. e65175.
108. Mann, D.M.A. and M.M. Esiri, *The pattern of acquisition of plaques and tangles in the brains of patients under 50 years of age with Down's syndrome*. J. Neurol. Sci., 1989. **89**: p. 169-179.
109. Wisniewski, K., Howe, J., Williams, G., and Wisniewski, H.M., *Precocious aging and dementia in patients with Down's syndrome*. Biological Psychiatry, 1978. **13**(5): p. 619-627.

110. Wisniewski, K., H. Wisniewski, and G. Wen, *Occurrence of neuropathological changes and dementia of Alzheimer's disease in Down's syndrome*. *Ann. Neurol.*, 1985. **17**: p. 278-282.
111. Rumble, B., et al., *Amyloid A4 and its precursor in Down's syndrome and Alzheimer's disease*. *New Engl. J. Med.*, 1989. **320**: p. 1446-1462.
112. Iturria-Medina, Y., et al., *Early role of vascular dysregulation on late-onset Alzheimer's disease based on multifactorial data-driven analysis*. *Nat Commun*, 2016. **7**: p. 11934.
113. Blanc, E.M., et al., *Amyloid beta-peptide induces cell monolayer albumin permeability, impairs glucose transport, and induces apoptosis in vascular endothelial cells*. *J Neurochem*, 1997. **68**(5): p. 1870-81.
114. Frost, J.L., et al., *Pyroglutamate-3 amyloid-beta deposition in the brains of humans, non-human primates, canines, and Alzheimer disease-like transgenic mouse models*. *Am J Pathol*, 2013. **183**(2): p. 369-81.
115. Buss, L., et al., *Intracerebral haemorrhage in Down syndrome: protected or predisposed?* *F1000Res*, 2016. **5**.
116. Hoffman, J.D., et al., *Age Drives Distortion of Brain Metabolic, Vascular and Cognitive Functions, and the Gut Microbiome*. *Front Aging Neurosci*, 2017. **9**: p. 298.
117. Parikh, I., et al., *Caloric restriction preserves memory and reduces anxiety of aging mice with early enhancement of neurovascular functions*. *Aging (Albany NY)*, 2016. **8**(11): p. 2814-2826.
118. Abrahamson, E.E., et al., *Cerebral blood flow changes after brain injury in human amyloid-beta knock-in mice*. *J Cereb Blood Flow Metab*, 2013. **33**(6): p. 826-33.
119. Lin, A.L., et al., *Chronic rapamycin restores brain vascular integrity and function through NO synthase activation and improves memory in symptomatic mice modeling Alzheimer's disease*. *J Cereb Blood Flow Metab*, 2013. **33**(9): p. 1412-21.
120. Struys, T., et al., *In vivo evidence for long-term vascular remodeling resulting from chronic cerebral hypoperfusion in mice*. *J Cereb Blood Flow Metab*, 2016.
121. Liu, S., et al., *Determination of Brain-Regional Blood Perfusion and Endogenous cPKCgamma Impact on Ischemic Vulnerability of Mice with Global Ischemia*. *Neurochem Res*, 2017. **42**(10): p. 2814-2825.
122. Muir, E.R., Q. Shen, and T.Q. Duong, *Cerebral blood flow MRI in mice using the cardiac-spin-labeling technique*. *Magn Reson Med*, 2008. **60**(3): p. 744-8.
123. Lei, H., et al., *Continuous arterial spin labeling of mouse cerebral blood flow using an actively-detuned two-coil system at 9.4T*. *Conf Proc IEEE Eng Med Biol Soc*, 2011. **2011**: p. 6993-6.
124. Chugh, B.P., et al., *Robust method for 3D arterial spin labeling in mice*. *Magn Reson Med*, 2012. **68**(1): p. 98-106.
125. Gao, Y., et al., *Arterial spin labeling-fast imaging with steady-state free precession (ASL-FISP): a rapid and quantitative perfusion technique for high-field MRI*. *NMR Biomed*, 2014. **27**(8): p. 996-1004.
126. Bothe, H.W., W. Bodsch, and K.A. Hossmann, *Relationship between specific gravity, water content, and serum protein extravasation in various types of vasogenic brain edema*. *Acta Neuropathol*, 1984. **64**(1): p. 37-42.

127. Rohrer, M., et al., *Comparison of magnetic properties of MRI contrast media solutions at different magnetic field strengths*. Invest Radiol, 2005. **40**(11): p. 715-24.
128. Ahlgren, A., et al., *Improved calculation of the equilibrium magnetization of arterial blood in arterial spin labeling*. Magn Reson Med, 2018.
129. Mutsaerts, H.J., et al., *Gray matter contamination in arterial spin labeling white matter perfusion measurements in patients with dementia*. Neuroimage Clin, 2014. **4**: p. 139-44.
130. Bester, M., et al., *Increased perfusion in normal appearing white matter in high inflammatory multiple sclerosis patients*. PLoS One, 2015. **10**(3): p. e0119356.
131. Sowa, P., et al., *Reduced perfusion in white matter lesions in multiple sclerosis*. Eur J Radiol, 2015. **84**(12): p. 2605-12.
132. van Dalen, J.W., et al., *White Matter Hyperintensity Volume and Cerebral Perfusion in Older Individuals with Hypertension Using Arterial Spin-Labeling*. AJNR Am J Neuroradiol, 2016.
133. Wright, S., et al., *Accelerated white matter aging in schizophrenia: role of white matter blood perfusion*. Neurobiol Aging, 2014. **35**(10): p. 2411-2418.
134. Thalman, S.W., D.K. Powell, and A.L. Lin, *Novel Calibrated Short TR Recovery (CaSTRR) Method for Brain-Blood Partition Coefficient Correction Enhances Gray-White Matter Contrast in Blood Flow Measurements in Mice*. Front Neurosci, 2019. **13**: p. 308.
135. Iglesiast, J.E., et al., *Simultaneous Bayesian correction of slab boundary artifacts and bias field for high resolution ex vivo MRI*. 2016. p. 1384-1387.
136. Lijnema, T.H., et al., *Gravimetric determination of the water concentration in whole blood, plasma and erythrocytes and correlations with hematological and clinicochemical parameters*. Clinica Chimica Acta, 1993. **214**(2): p. 129-138.
137. Cohen, J., *Statistical power analysis for the behavioral sciences*. 2nd ed. ed. 1988, Hillsdale, N.J.: Hillsdale, N.J. : L. Erlbaum Associates.
138. MGH. *FreeSurfer Suggested Morphometry Protocols*. 2009 [cited 2019 April 29]; Available from: http://surfer.nmr.mgh.harvard.edu/fswiki/FreeSurferWiki?action=AttachFile&do=get&target=FreeSurfer_Suggested_Morphometry_Protocols.pdf.
139. Styner, M., et al., *Parametric estimate of intensity inhomogeneities applied to MRI*. IEEE Transactions on Medical Imaging, 2000. **19**(3): p. 153-165.
140. Wells, W.M., et al., *Adaptive segmentation of MRI data*. IEEE Transactions on Medical Imaging, 1996. **15**(4): p. 429-442.
141. Tofts, P.S., *PD: Proton Density of Tissue Water*, in *Quantitative MRI of the Brain*. 2003.
142. Rosenberg, G.A., *Ischemic brain edema*. Progress in Cardiovascular Diseases, 1999. **42**(3): p. 209-216.
143. Niemoller, U.M. and M.G. Tauber, *Brain edema and increased intracranial pressure in the pathophysiology of bacterial meningitis*. Eur J Clin Microbiol Infect Dis, 1989. **8**(2): p. 109-17.
144. Winkler, E.A., et al., *Cerebral Edema in Traumatic Brain Injury: Pathophysiology and Prospective Therapeutic Targets*. Neurosurg Clin N Am, 2016. **27**(4): p. 473-88.

145. Aleksis, R., et al., *Structural studies of amyloid-beta peptides: Unlocking the mechanism of aggregation and the associated toxicity*. Biochimie, 2017. **140**: p. 176-192.
146. Bobinski, M., et al., *The histological validation of post mortem magnetic resonance imaging-determined hippocampal volume in Alzheimer's disease*. Neuroscience, 1999. **95**(3): p. 721-725.
147. Duning, T., et al., *Dehydration confounds the assessment of brain atrophy*. Neurology, 2005. **64**(3): p. 548-50.
148. Jimenez, C., et al., *Plasma volume changes during and after acute variations of body hydration level in humans*. Eur J Appl Physiol Occup Physiol, 1999. **80**(1): p. 1-8.

VITA

Scott William Thalman

Education:

University of Kentucky, Lexington, KY
College of Medicine, Aug. 2012-present
GPA, 3.81
USMLE Step 1, 238 (65th percentile)

F. Joseph Halcomb III, MD Dept. of Biomedical Engineering Aug. 2014-present
GPA, 4.0

Brigham Young University, Provo, UT
B.S. Applied Physics, Cum Laude Aug. 2011
Minor in Mathematics with a Pre-Medical Emphasis
Senior Thesis: Photoluminescence Lifetimes of InGaAs and CdSe Quantum Dots
GPA 3.83, MCAT 38 (98th percentile)

Research Experience:

Graduate Research Assistant May 2016-present
Lin Brain Lab, Univ. of Kentucky Dept. of Biomedical Engineering
Primary investigator – Dr. Ai-Ling Lin

Graduate Research Assistant Aug. 2014-May 2016
Vandsburger Lab, Univ. of Kentucky Dept. of Biomedical Engineering
Primary investigator – Dr. Moriel Vandsburger

Undergraduate Research Assistant Apr. 2009-Oct. 2011
Brigham Young University Department of Physics and Astronomy
Primary investigator- Dr. John S. Colton

Undergraduate Research Assistant Aug. 2010-Oct. 2011
University of Utah Hospital Department of Surgery
Primary investigator- Dr. Edward Kimball

Volunteer Experience:

Emergency Department Volunteer May 2011-Oct. 2011
University of Utah Hospital Emergency Department
Supervisor- Tracy Bodrero

Student-Athlete 2005-2006, 2008-2010
Brigham Young University NCAA Division I Diving Team

Coach – Keith Russel

Volunteer Missionary

2006-2008

Church of Jesus Christ of Latter Day Saints – Paris, France
President Steven Pond

Publications

- “Brain-Blood Partition Coefficient and Cerebral Blood Flow in Canines Using Calibrated Short TR Recovery (CaSTRR) Correction Method.” Thalman S.W., Powell D.K., Ubele M., Head E., Lin, A.L., *In Preparation*
- “Global Cerebral Blood Flow in People with Down Syndrome: an Arterial Spin Labeling Study.” Thalman S.W., Lin A.L., Helman A., Johnson N.F., Andersen A., McCarty K., Davis R., Jicha G., Caban-Holt A., Robertson W., Lightener D., Powell D.K., Head E., Schmitt F., *In Preparation*
- “Novel Calibrated Short TR Recovery (CaSTRR) Method for Brain-Blood Partition Coefficient Correction Enhances Gray-White Matter Contrast in Blood Flow Measurements in Mice.” Thalman S.; Powell D.K.; Lin, A.L., *Front Neurosci* 2019 **13**:308
- “Advanced Cardiac Chemical Exchange Saturation Transfer (cardioCEST) - MRI for Multi-Color Cell Tracking and Metabolic Imaging.” Pumphrey, A.; Yang, Z.; Ye, S.; Thalman, S.W.; Watt, D.; Abdel-Latif, A.; Unrine, J.; Thompson, K.; Fornwalt, B.; Ferrauto, G.; Vandsburger, M. *NMR Biomed* 2016 **29**(1):74-83.
- “Assemblies composed of oligothiophene-ruthenium complexes bound to CdSe nanoparticles,” N. Bair, J.M. Hancock, C.J. Simonson, S.W. Thalman, J.S. Colton, M.C. Asplund, R.G. Harrison, *Journal of Luminescence* 158(2):501-509
- “Growth and temperature dependent photoluminescence of InGaAs quantum dot chains,” H. Yang, D.J. Kim, J.S. Colton, T. Park, D. Meyer, A.M. Jones, S.W. Thalman, D. Smith, K. Clark, S. Brown, *Applied Surface Science* 296(3):8-14
- “Universal scheme for measuring the electron T1 in semiconductors and application to a lightly-doped -GaAs sample,” J.S. Colton, K. Clark, D. Meyer, T. Park, D. Smith, S.W. Thalman, *Solid State Comm.* 152(3):410-413
- “Photoluminescence Lifetimes of Quantum Dots,” S.W. Thalman, senior thesis for BS in Applied Physics from Brigham Young University (March 2011)

Abstracts and Presentations

- “Global Cerebral Blood Flow in People with Down Syndrome: an Arterial Spin Labeling Study.” Thalman S.W., Lin A.L., Helman A., Johnson N.F., Andersen A., McCarty K., Davis R., Jicha G., Caban-Holt A., Robertson W., Lightener D., Powell D.K., Head E., Schmitt F., “Blood-Brain Partition Coefficient Correction Improves Gray-White Matter Contrast in Blood Flow Measurement in Mice.” Thalman, S.W.; Powell D.; Lin, A.L., 2019 *Univ. Ky CCTS Spring conference*, Oral Presentation
- “Blood-Brain Partition Coefficient Correction Improves Gray-White Matter Contrast in Blood Flow Measurement in Mice.” Thalman, S.W.; Powell D.; Lin, A.L., *ISMRM Annual Meeting*, June 2018

- “Blood-Brain Partition Coefficient Correction Improves Gray-White Matter Contrast in Blood Flow Measurement in Mice.” Thalman, S.W.; Powell D.; Lin, A.L., 2018 *Univ. Ky CCTS Spring conference*, Oral Presentation
- “Using Calibrated Proton Density Imaging to Measure Blood-Brain Partition Coefficient in Aging and Alzheimer’s Disease Mice.” Thalman, S.W.; Powell D.; Shen, A.; Hartz, A.; Lin, A.L., Poster Presentation, *ISMRM Annual Meeting*, April 2017, Poster Presentation
- “Calibrated Proton Density Imaging Measures Reduced Blood-Brain Partition Coefficient in Aging Mice.” Thalman, S.W.; Powell D.; Lin, A.L., Oral Presentation, *ISMRM Workshop on Quantitative MR Flow*, Oct, 2016
- “The Effect of Hypertrophy in CardioCEST Magnetization Transfer Contrast.” Thalman, S.W.; Pumphrey, A.; Yang, Z.; Vandsburger, M., Poster Presentation, *Proc. ISMRM Annual Meeting* May, 2016
- “Cardiac CEST Imaging of Diffuse Fibrosis.” Thalman, S.W.; Yang, Z.; Mattingly, A.; Vandsburger, M., Poster Presentation, *Proc. ISMRM Annual Meeting* June, 2015
- “Photoluminescence Lifetime Measurements of Indium Gallium Arsenide Quantum Dot Structures Using Time-Correlated Single Photon Counting,” S.W. Thalman, J.S. Colton, H. Yang, Presentation at the Annual Meeting of the Four Corners Section of the APS (October 2010), Oral Presentation

Awards and Honors

ISMRM Magna Cum Laude Merit Award for Outstanding Poster Presentation	2019
T32 Predoctoral fellowship, T32AG057461	2017-19
ISMRM Annual Meeting Travel Stipend Award	2018
ISMRM Annual Meeting Travel Stipend Award	2017
F. Joseph Halcomb III, MD Fellowship for Engineering in Medicine	2015-17
ISMRM Workshop on Quantitative MR Flow Travel Stipend	2016
Gill Heart Institute Annual Research Day, Outstanding Graduate Poster Award	2015
ISMRM Annual Meeting Travel Stipend Award	2015
Mountain West Conference Scholar-Athlete Award	2010
Mountain West Conference Scholar-Athlete Award	2009
Mountain West Conference Scholar-Athlete Award	2006
Robert C. Byrd Scholarship, Colorado Dept. of Education	2005
Brigham Young University President’s Scholarship	2005